STIMULUS FREQUENCY DEPENDENCY OF POST STIMULUS UNDERSHOOT OF THE BOLD fMRI SIGNAL

by

Ahmet Sabri Alper

Doctor of Medicine, Celal Bayar University, 2005

Submitted to the Institute of Biomedical Engineering
in partial fulfillment of the requirements
for the degree of
Master of Science
in
Biomedical Science

Boğaziçi University
January 2008

ACKNOWLEDGMENTS

I am greatly thankful to Assoc. Prof. Dr. Cengizhan Öztürk, for his supervising, encouragement, support and endless motivation. He was the one to hand me the BUMIL lab keys from day one, never had a frown on his face although when things did not go as expected and always had an open door policy even when he was out of the country.

I would like to thank to Uzay Emrah Emir for introducing me to the topic, his support, help and guidance throughout my thesis progress. I wish him the best of luck with his new adventure in the US. Ali Bayram from BUMIL was also very helpful when conducting the experiments at the NPIstanbul hospital. I very much appreciate his extra time spent for my thesis, and thank NPI for letting me use their MR facilities.

I am indebted to all of my experiment subjects, who spent 2 hours inside the MR machine, in an experiment setup which might as well be considered a legal way of torture.

I will always be grateful to my parents and my sister for always pointing me to the right direction, their support, and love.

It would not have been possible for me to complete this thesis on time, if it weren't for my dear wife. I thank her the most for her patience, love and trust in me.

ABSTRACT

STIMULUS FREQUENCY DEPENDENCY OF POST STIMULUS UNDERSHOOT OF THE BOLD fMRI SIGNAL

The aim of this study is to investigate the effects of different stimulation frequencies on post stimulus undershoot of the blood oxygen level dependent functional magnetic resonance imaging signal. A fiber optic light delivery system connected to a black opaque sunglass is constructed to deliver visual stimuli to subjects during fMRI scans. One static visual stimulus and eleven flashing stimuli with frequencies ranging from 4 to14Hz and 30 to 46Hz are applied one subject in one fMRI scan session.

The acquired data is analysed to obtain the BOLD fMRI parameters. Positive blood oxygen level dependent and post stimulus undershoot signal changes in the primary visual cortex are determined for each frequency. The results suggest that the post stimulus undershoot has a frequency dependency independent of cerebral blood volume changes. Requirement of more data and additional measures for following possibly related phenomena such as cerebral blood flow are discussed which might be investigated in further studies.

Keywords: fMRI, BOLD, PSU, Visual Cortex

ÖZET

BOLD fMRG SİNYALİNİN UYARAN SONRASI DİBEATIMININ FREKANS BAĞIMLILIĞI

Bu çalışmanın amacı, farklı uyaran frekanslarının, kan oksijen seviyesine bağımlı fonksiyonel manyetik rezonans görüntüleme sinyalinin uyaran sonrası dibeatımına etkilerinin araştırılmasıdır. fMRG çekimleri sırasında deneklere görsel uyaranları iletmek amacıyla siyah, opak bir güneş gözlüğüne bağlı fiber optik ışık iletim sistemi kuruldu. Bir statik, 4-14Hz ve 30-46Hz aralığında 11 değişik frekansta yanıp sönen görsel uyaran, sağlıklı bir deneğe bir fMRG çekim oturumunda uygulandı.

Alınan veriler analiz edilerek BOLD fMRG parametreleri elde edildi. Her frekans için birincil görme alanındaki pozitif BOLD ve PSU sinyal değişimleri belirlendi. Elde edilen sonuçlar PSU'nun serebral kan hacmindeki değişimlerden bağımsız bir frekans bağımlılığı olduğunu işaret etmektedir. Sonuçlar, daha fazla verinin gerekliliği ve serebral kan akımı gibi muhtemelen konu ile alakalı değişkenlerin de hesaplanması için atılabilecek adımlar tartışıldı.

Anahtar Sözcükler: fMRG, BOLD, PSU, birincil görme alanı.

TABLE OF CONTENTS

LIST OF FIGURES

LIST OF TABLES

LIST OF SYMBOLS

Hz	Hertz
Na	Sodium
K	Potassium
s	Second
T	Tesla
γ	Gyromagnetic Ratio

LIST OF ABBREVIATIONS

ASL	Arterial Spin Label
BOLD	Blood Oxygen Level Dependent
CBF	Cerebral Blood Flow
CBV	Cerebral Blood Volume
$CMRO_2$	Cerebral Metabolic rate of Oxygen
CPU	Central Processing Unit
CSF	Cerebrospinal Fluid
CT	Computed Tomography
EEG	Electroencephalography
EPI	Echo Planar Imaging
FID	Free Induction Decay
fMRI	Functional Magnetic Resonance Imaging
fNIRS	Functional Near Infrared Spectroscopy
GE	Gradient Echo
HbO	oxy-Hemoglobin
HbR	deoxy-Hemoglobin
MEG	Magnetoencephalography
MRI	Magnetic Resonance Imaging
NMR	Nuclear Magnetic Resonance
PET	Positron Emission Tomography
PSU	Post Stimulus Undershoot
RF	Radio Frequency
SE	Spin Echo
SNR	Signal to Noise Ratio
SPECT	Single Photon Emission Computed Tomography

1. INTRODUCTION

1.1 Motivation and Objectives

The human brain is the most complex and yet the least understood organ of the body. The main reason aside from it being complex, is probably because there were not many noninvasive diagnostic approaches to assess the functions of the brain and the anatomical locations in the brain which those functions took place.

Early studies for mapping brain functions non-invasively could only be done on patients who had sustained severe injuries to the head. Based on the location and severity of the injury, and comparing it to the loss of function, one could infer the location of the brain that was responsible for the lost function. There were invasive animal studies and even surgical operations on humans took place to cure "madness".

In spite of the advances in the medical and biomedical fields, it was hard to conduct experiments on healthy subjects to assess brain functions. However, with the recent advances in neuroimaging modalities - which will be further discussed on the next chapters- it is now possible to map the brain to an extent, diagnose illnesses and maybe even help people bypass their disabilities by measuring and assessing the blood oxygen level dependent (BOLD) functional magnetic resonance imaging (fMRI) signal.

BOLD fMRI is used to measure neuronal metabolic activity at high spatial resolution without the use of any contrast agent [16]. BOLD fMRI signal during the neuronal activity is the combined effects of several physiological parameters such as: cerebral blood flow (CBF), cerebral blood volume (CBV) and cerebral metabolic rate of oxygen ($CMRO_2$) [17, 18]. Effects of these physiological parameters, alone or in combination, also with the type and specifics of the stimulus presented can be responsible

for the final shapes of the three transients in the BOLD response. These transients are namely an initial dip, positive BOLD and the post stimulus undershoot which is the main concern of this thesis.

Intrasubject and intersubject differences in the amplitude and duration of these transients are thought to be reflecting differences in the hemodynamic coupling and/or differences in neuronal activity [19, 20, 18]. Temporal frequency dependency of PBOLD and CBF based fMRI has been well studied in previous researches [20, 21, 22, 23, 24]. It has been reported in such studies that an increase in PBOLD up to 8 Hz is followed either by a decrease or a plateau with higher frequencies. These results are also in agreement with early PET studies [25, 26].

So far, most of the studies related to stimulus rate response were based on PBOLD. An interesting question that still remains unanswered is how PSU, which is commonly observed in fMRI studies, effectively responds to different stimulation rates. This study tries to address this question by assessing the response of PSU to different stimulation frequencies by block design fMRI technique.

1.2 Outline of the Thesis

There are five chapters following this one in the thesis. In the next chapter information and a literature survey about the history of neuroimaging, and brief introductions to current neuroimaging modalities are given. The principles of magnetic resonance imaging are discussed in chapter 3. Chapter 4 includes the physiological basis of the BOLD signal and some of the hypotheses on the transients of the BOLD signal, such as the post stimulus undershoot. The study design and fMRI data acquisition and analysis are discussed in chapter 5 with the results of the study. Finally the results are discussed with possible thoughts on future work are given in chapter 6.

2. A BRIEF HISTORY OF NEUROIMAGING

2.1 Introduction

Brain, the most important yet the least understood part of the human body is the counterpart of what central processing unit (CPU) is to a computer. The CPU requires energy and other resources like cooling, which is provided by the control of the main board via a wire based delivery system. As the function, the computer is undertaking gets tougher, the energy demand of the CPU increases and the main board provides.

Like its counterpart the brain requires energy and other resources to function. Heart is the main board that pumps glucose and oxygen within the blood to the brain via vessels to let it produce its energy. As the task, the brain is trying to accomplish gets tougher, more supplies are delivered to the site of action with blood.

So it can be thought that as the task a specific part of the body undertakes gets tougher, the amount of blood it receives at a time increases -and the brain gets the priority for obvious reasons. However, this was not known nor accepted in the scientific community until 1928 [27] and it took even more before a quantitative method for measuring whole brain blood flow and metabolism in humans was developed [28, 29, 30]. Still, there are many unanswered questions about the functioning of the human brain.

This chapter focuses on some of the neuroimaging modalities which have been used to assess the brain structure and functions.

2.2 Pneumoencephalography and Cerebral Angiography

The first "serious" step in the history of neuroimaging came with a technique named pneumoencephalography in 1919. This technique was discovered by a neurosurgeon, Walter Dandy. The procedure involved draining some of the cerebrospinal fluid from around the brain via lumbar spinal puncture and replacing it with air, oxygen, or helium to allow the structure of the brain to show up more clearly on X-ray images. It is derived from ventriculography, an earlier and a more primitive modality where the air is injected through holes drilled in the skull.

Pneumoencephalography had been used widely since its discovery, but its use was abandoned in 1980s with the development of new neuroimaging techniques. The actual procedure was extremely dangerous and came with common side effects like headaches and vomiting. Also the replacement of the drained spinal fluid took a long time resulting in a long recovery period of a few months.

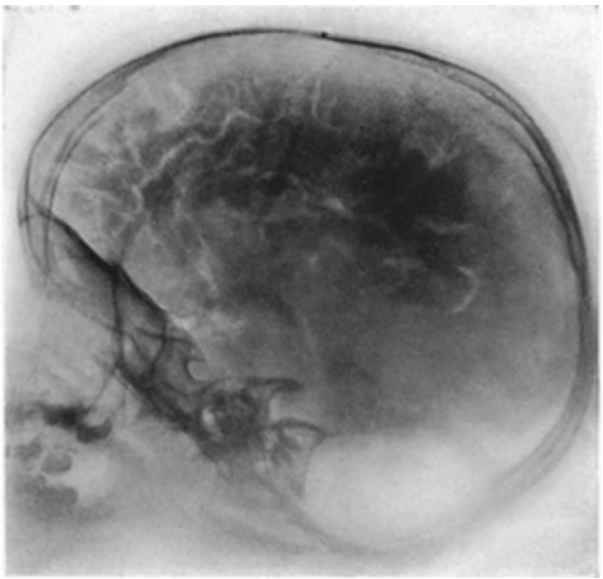

Figure 2.1 Photograph of a roentgenogram of the head after an intraspinous injection of the air (pneumoencephalography procedure). The brain sulci and cisterna are visible. Reproduced from [1].

In 1927, Egas Moniz who is one of the pioneers of leucotomy -later known as

lobotomy- developed a technique to visualize arteries and veins in the brain. The technique is called cerebral angiography and involves passing of a catheter through a large artery and to the carotid artery. As the catheter is in place, a radio-opaque contrast material is introduced into the cerebral blood stream followed by a series of radiographs taken when the contrast agent is passing and after it has passed through the tissues.

The result of these radiographs provides the visual map of cerebral blood vessels in and around the brain which helps physicians to diagnose a variety of neurological disorders such as arteriovenous malformations and tumors. This technique is still in use today also with its less invasive counterparts like cerebral computed tomography angiography and magnetic resonance angiography.

Figure 2.2 Cerebral angiography image. Reproduced from [2].

2.3 Electroencephalography and Magnetoencephalography

Another doctor, Hans Berger focusing on brain circulation was also interested in the works of a British scientist, Richard Caton who reported to the British Medical Association that he had used a galvanometer to observe electrical impulses from the

surfaces of living brains in animal subjects [31]. Following the work of Caton in animals and applying a similar method on humans, Berger made the first electroencephalogram recording in humans and called it Electroenkephalogram (EEG) [32].

Using the EEG he was also the first to describe the different waves which were present in the normal and abnormal brain, such as the alpha wave rhythm (8-12 Hz). Quoting from his article's translation: "Caton has already published experiments on the brains of dogs and apes in which bare unipolar electrodes were placed either on the cerebral cortex and the other on the surface of the skull. The currents were measured by a sensitive galvanometer. There were found distinct variations in current, which increased during sleep and with the onset of death strengthened, and after death became weaker and then completely disappeared." [33].

Clinically EEG is recorded using silver coated with silver chloride electrodes attached to the scalp and kept in good electrical contact with the help of conductive electrode gel. One or more active sites may be monitored relative to a reference electrode placed on an area of low response activity like the earlobe. The signals received are in the order of microvolts so external interference, eye movements and muscle twitches should be taken into consideration. Aside from Alpha waves, mainly beta, theta and delta waves are also distinguished which are used in diagnosis and monitoring of the brain.

The EEG has changed little since its first applications in humans, however it is now also used in a more range of areas then to just providing a characteristic tracing of life to demonstrating its absence. For example, the EEG can be measured after a repeating visual stimulus or after memory exercises. The responses to the stimuli collected by each electrode is recorded and averaged over a number of trials. The latency of the peak of the signal from the stimulus presentation characterizes the response. Now that an electrical signal of interest is found, the magnitude of the peak is mapped across the scalp giving an idea of the source. However, since the signals are

measured on the scalp, they may not be representing the activity in the underlying cortex. In order to generate a signal that is detectable via EEG, around 50,000 active neurons are needed [34]. This limitation is a major disadvantage to the use of EEG however it has advantages like continuous monitoring during sleep, low cost and being safe.

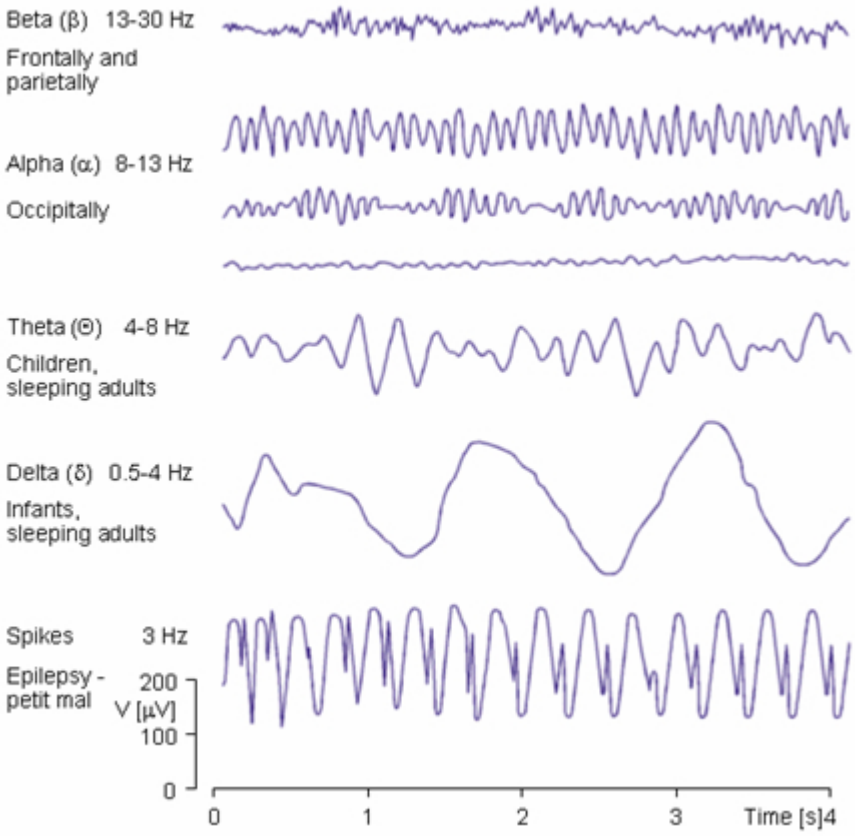

Figure 2.3 Some examples of EEG waves. Reproduced from [3].

The EEG signals derive from the net effect of ionic currents flowing in the dendrites of neurons during synaptic transmission. Considering Maxwell's equations [35], any electrical current will produce an orthogonally oriented magnetic field. And that field produced in the brain was first measured by David Cohen in 1968 [36]. The first measurements were made using only a copper induction coil as the detector, in a magnetically shielded room which reduced magnetic background noise. The results taken were still too noisy until superconducting quantum interference devices (SQUID)

were used as the detector. Within a better shielded room and with the help of the highly sensitive SQUID detector, Cohen was able to take measurements almost as clear as EEG signals giving rise to magnetoencephalography [37].

MEG can be considered as a totally non-invasive modality and can help in the measurement of time courses of activity and pinpointing sources in primary auditory, somatosensory and motor areas [38, 39]. However its use is more limited in creating functional maps of human cortex during more complex cognitive tasks. Also it is still not possible to successfully detect and locate signals originating from the non-cortical parts of the brain [40]. Its very high cost hits the final blow on limiting its clinical use today.

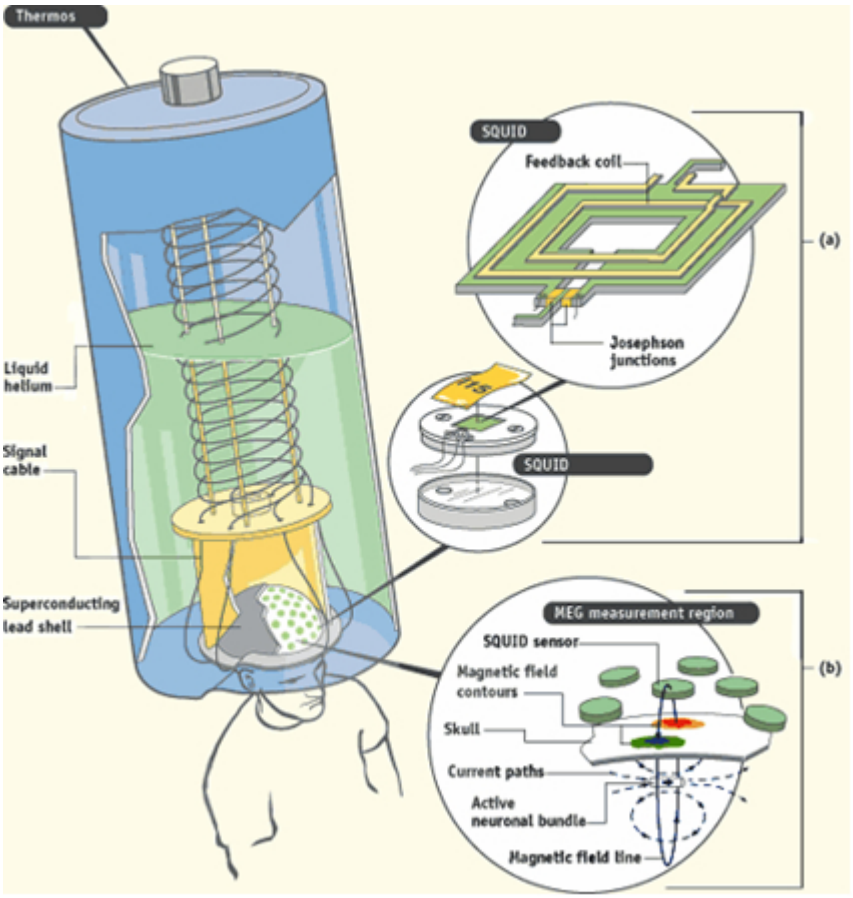

Figure 2.4 Schematics of a MEG helmet array [4].

As the EEG was discovered, scientists could understand more about the state of the brain, however it was still a great desire in the scientific community to better display and store the images of actual, living brain by imaging methods. The answer to this question had its roots in the discovery of x-rays by Wilhelm Conrad Roentgen in 1895.

2.4 Computed Tomography

Since standard radiographs were not able to give a clear picture of what was inside the skull, Godfrey Newbold Hounsfield, using x-rays originating from different angles managed to acquire the image of his brain in slices. His work on this area had begun in late 1960s, patented the first device in 1972 and notified the world of his discovery which would open a new era in diagnostic imaging in 1973 [41], the computerized axial scanning, later to be known as Computed Tomography. The combination of a moving x-ray gantry and the computing algorithms and power necessary to reconstruct from projections made CT possible.

Tomography refers to the cross-sectional imaging of an object from either transmission or reflection data collected by illuminating the object from many different directions. The impact of this technique in diagnostic medicine has been revolutionary, since it has enabled doctors to view internal organs with unprecedented precision and safety to the patient. [42].

Siemens was the first medical equipment manufacturer to produce a CT device, SIRETOM in 1974. From then, the use of CT in hospitals grew exponentially and CT is today one of the most important diagnostic tools in use.

Figure 2.5 Computed tomography (CT) image of the brain (without contrast material) demonstrates a 3x3x4 cm high-attenuation mass (arrows) within the right temporal lobe. Reproduced from [5].

2.5 Single Photon Emission Tomography and Positron Emission Tomography

About a few months after Roentgen's discovery of x-rays, Becquerel and the Curies were discovering radioactivity and radium in 1896, resulting in the possibility of the future development of nuclear medicine. About half a century later, Anger discovered the Gamma camera in 1958. Gamma camera is a device used to view and analyze images of the human body of the distribution of medically injected, inhaled, or ingested gamma ray emitting radionuclides [6]. This finally resulted in the discovery of Single Photon Emission Computed Tomography (SPECT).

As its name suggests (single photon emission), gamma-ray emissions are the source of information, rather than x-ray transmissions as used in conventional Computed Tomography. The Gamma camera collects gamma rays that are emitted from

within the patient by the decaying radioactive isotope, allowing the reconstruction of a picture of where the gamma rays originated. In SPECT the gamma camera is not stationary over the patient but is rotating around the patient allowing the reconstruction of 3D images. From this, one can determine how a particular organ or system is functioning on a 3D display.

From the aspect of neuroimaging SPECT is mainly used for measuring regional cerebral blood flow which is tightly coupled to regional brain metabolism and energy use. This accomplishes the task of Kety and Schmidt who back in 1948 used nitrous oxide as an indicator to measure the difference between arterial input and venous outflow which could only account for the total -not regional- cerebral blood flow. SPECT is also used partly experimentally in the diagnosis and differential diagnosis of Alzheimer's disease and other dementias with technetium-99m as the radioisotope of choice [43, 44].

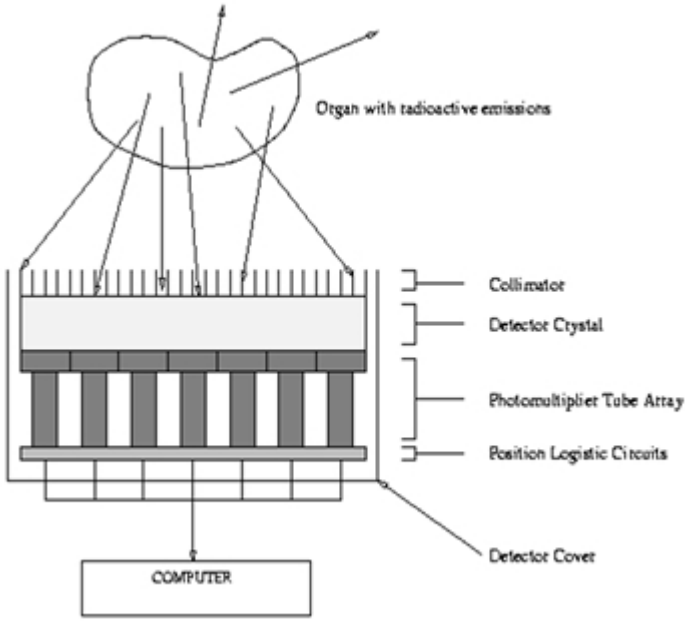

Figure 2.6 Schematics of a gamma camera [6].

In 1975, just two years after Hounsfield's CT discovery, Ter-Pogossian and colleagues came up with Positron Emission Tomography (PET) [45]. Like in SPECT a radioisotope is provided to the subject. But this short-lived radioisotope is chemically

integrated into a metabolically active molecule like fluorodeoxyglucose (FDG) and is injected to the patient. Instead of directly emitting gamma rays, the radioisotope used in PET studies decays by emitting positrons which then annihilate with an electron around. This annihilation results in a pair of photons traveling 180 degrees away from each other. As the pairs reach the detector rings they are accounted for in a ring of scintillators and photomultiplier tubes surrounding the gantry, the rest is handled by the coincidence processors and computers to reconstruct images of metabolic activity in space.

Cancer cells require a great deal of glucose, to have enough energy to grow. PET scanning utilizes a radioactive molecule that is similar to glucose, called fluorodeoxyglucose (FDG). FDG accumulates within malignant cells because of their high rate of glucose metabolism. Once injected with this agent the patient is imaged on the whole body PET scanner to reveal cancer growths which may have been overlooked or difficult to characterize by conventional CT, X-Ray, or MRI.

Although very much useful, PET's applications does not end with "only" cancer detection or the research in dementias. Mainly beginning with a study published in 1984, where ^{15}O-labeled water is injected to 8 subjects over a series of 56 measurements, Fox and friends used an adaptation of the Kety autoradiographic model to the study of functional-anatomical correlations within the human brain. They were able demonstrate that quantitative functional brain mapping did not require the determination of regional cerebral blood flow (rCBF) from regional tissue radiotracer concentration (Cr) when regional neuronal activation was expressed as the change in rCBF from an initial, resting-state measurement [46].

Since then functional-anatomical correlations within the human brain are thoroughly investigated with the help of PET. For instance, it is used to quantify regional cerebral glucose utilization which usually correlates with regional synaptic activity [47, 48], also PET helps in measuring regional cerebral blood volume (rCBV) and re-

gional cerebral blood flow (rCBF) with the help of ^{15}O-CO and ^{15}O-H_2O radiotracers.

However PET has some inherent disadvantages. Aside from the need of radiotracers which are basically metabolical compounds integrated with radionuclides, those radionuclides must be produced in a cyclotron. The radionuclides have very short half lives. So the cyclotron can not be very far from the PET facility, this alone adds more cost to PET studies.

Table 2.1
Some radionuclides used in PET studies and their approximate half lives.

Radionuclide	Approximate Half Life
Oxygen-15	2 minutes
Nitrogen-13	10 minutes
Carbon-11	20 minutes
Fluorine-18	110 minutes

Also, PET does not provide much useful information about the underlying anatomical structure, so it is preferably used in combination with a CT or MRI scan. Since co-registration of images taken at different times due to patient and organ movements are difficult, hybrid PET/CT devices are manufactured. This added "anatomy to PET's function" but did not help PET studies get cheaper, therefore did not make them much more available for research and for the clinical use.

Seventies were important years for neuroimaging as the first solid applications of CT and PET were introduced into the medical field, but it did not stop there.

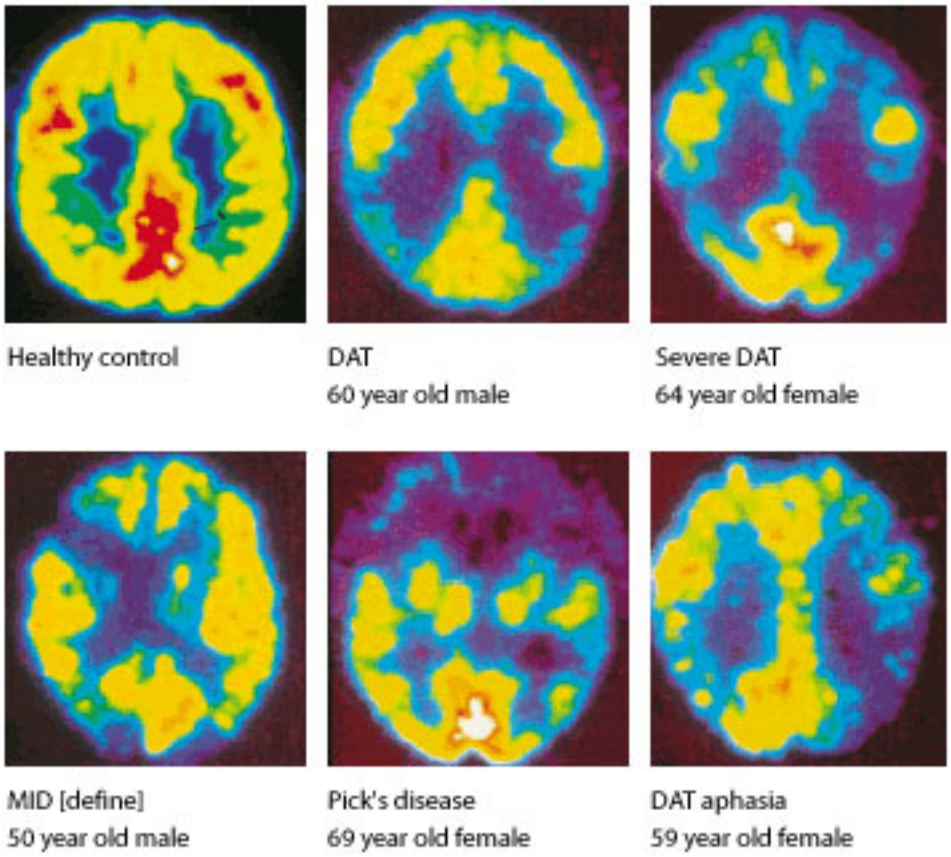

Figure 2.7 PET images of a dementia study (DAT: Dementia of the Alzheimer Type; MID: Multi-Infarct Dementia). Reproduced from [7].

2.6 Magnetic Resonance Imaging and Functional MRI

In 1946 soon after the end of World War II, "Nuclear Induction" was discovered by Purcell and Pound and independently by Bloch [49, 50]. What they discovered was that it was possible to detect a signal -or a voltage in a coil- when a sample was placed in a magnetic field and irradiated with radiofrequency (RF) energy of a certain frequency. That certain frequency is the resonant or namely the Larmor frequency and the signal is produced by the interaction of the sample's nuclei with the surrounding magnetic field. Later on Hahn practically "stumbled upon" the spin echoes [51], which is the basis of the spin echo pulse sequence currently being used in many of the clinical investigations made with MRI.

The research in nuclear magnetic resonance (NMR) continued throughout the years, contributed by scientists of many different fields as NMR was definitely a multi-disciplinary issue. But it wasn't until Ray Damadian's discovery in 1971, which the idea of using NMR in imaging of human body popped up. Damadian's discovery showed that certain tumors in rats displayed elevated relaxation times compared with normal tissues in vitro [52]. He later submitted a proposal to the US Patent and Trademark Office, the nuclear induction "Apparatus and method for detecting cancer in tissue" which was issued in 1974 with US patent 3789832.

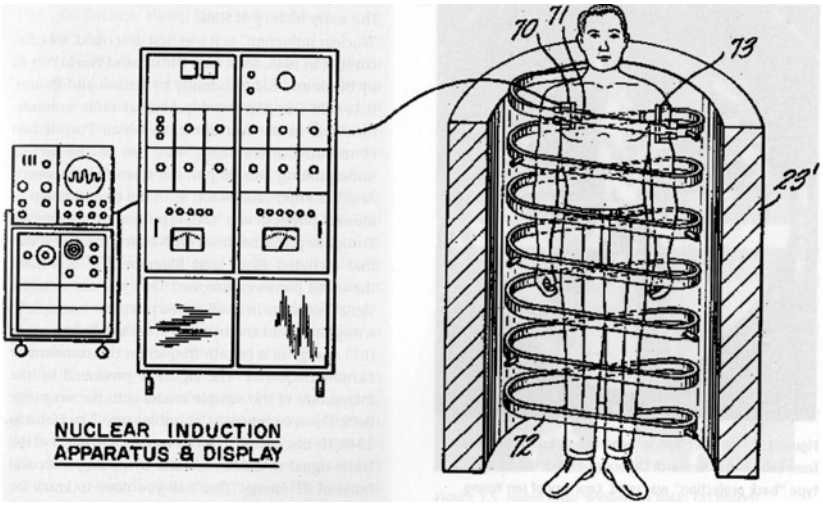

Figure 2.8 Raymond Damadian's "Apparatus and method for detecting cancer in tissue". US patent 3789832 filed 17 March 1972, issued 5 February 1974 [8].

Meanwhile, Paul Lauterbur proposed using magnetic field gradients to distinguish between NMR signals originating from different locations in 1973 [53], which became one of the fundamental roots of all modern MRI, the frequency encoding. He termed his invention "zeugmatography" meaning imaging from a joining together -of the main field and the gradients, but the name never became popular. Damadian named his technique FONAR (Field fOcused Nuclear mAgnetic Resonance)[54] and produced the first live whole body image in 1977 [55]. Later on the term "nuclear" was dropped as it was wrongly associated with ionizing radiation and also the psychological effects of World War II were still lingering.

The first commercial magnetic resonance imagers were built in the early 1980s, and the technique developed rapidly through the late 1980s to become the method of choice for non-trauma neurological scanning. Due to problems of low signal and high sensitivity to motion, whole body MR did not proceed much until the mid 1990s. The key factors being, the development of faster imaging techniques, particularly gradient echo and phased array coil technology [8].

Even if creation of a fully homogenous static magnetic field was practically possible, the heterogeneous nature of the human body would cause local inhomogeneities in the magnetic field. These field inhomogeneities first appeared in MR images as artifacts, like a distortion of the image or a reduction of the local MR signal. In the early 1990s, Ogawa et al. proposed that the oxygenation state of hemoglobin had a measurable effect on the signal measured by MR imaging [16]. Following this demonstration, Kwong et al. demonstrated the capability of mapping brain activity based on blood oxygenation changes related to neuronal activation [20]. This opened a new era of functional neuroimaging. This technique of functional magnetic resonance imaging (fMRI) has become a standard tool for neuroimaging and is now widely used for mapping the working human brain.

Now, MRI serves as a great tool to produce excellent anatomical detail and accomplishes this without the need of ionizing radiation like CT does. This has made MRI to become the method of choice for nontrauma neurological scanning and also secured a part in clinical radiology. Also with the constant research done in the field of fMRI, it has mostly replaced PET for studying the brain activation patterns with another advantage of not needing to rely on any external contrast material or radiotracers. Also being relatively non-invasive, makes MRI a highly repeatable diagnostic and research tool. NMR, MRI and fMRI concepts will be discussed further in the following sections of this document.

All techniques mentioned above has some disadvantages on displaying anatom-

ical details or in the measurement of hemodynamic, metabolic and electrical changes that take place during neuronal activities. However, combining these techniques helps in solving such problems, overcoming their limitations and sometimes confirming each other's results. For instance, as mentioned previously the PET/CT hybrid devices add anatomy to PET's functional studies. Also multimodality approaches in overcoming the spatial limitations of EEG and the temporal limitations of fMRI with their combined usage seems promising [56].

Finally, mentioning a PhD study which was conducted by Uzay Emir from BUMIL on the multimodal investigation of fMRI and functional near infrared spectroscopy (fNIRS) [57] would be another good example to stress how multimodality approaches are advantageous and to emphasize the importance of fMRI in functional neuroimaging studies.

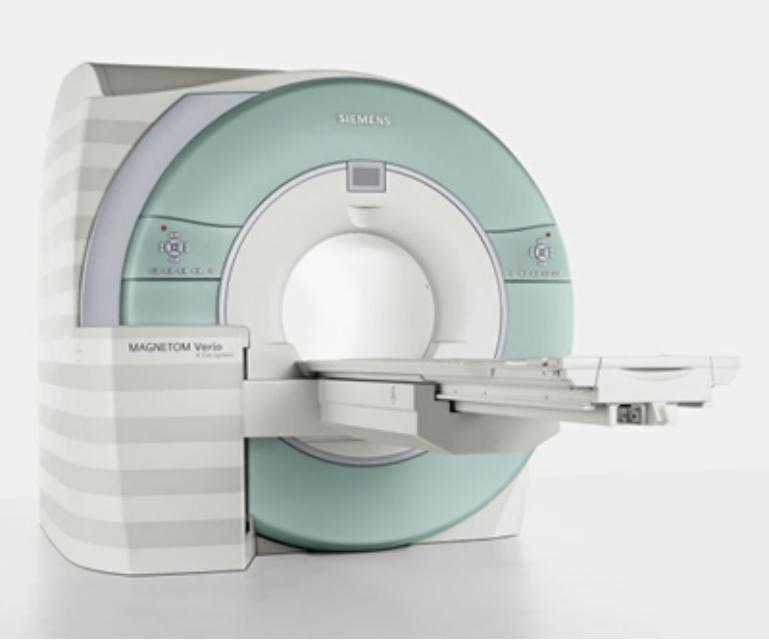

Figure 2.9 A modern 3T MR system from Siemens medical.

3. PRINCIPLES OF MAGNETIC RESONANCE IMAGING

3.1 Introduction

In this section, a brief overview will be given on the principles of NMR, followed by the basic principles of MRI. More information can be found in the related reference books [8, 15].

3.2 Nuclear Magnetic Resonance

3.2.1 Spin

The main particles, positively charged protons and uncharged neutrons held together by nuclear forces composing the nucleus of an atom possess an intrinsic quantum mechanical property, the angular momentum called spin. All protons and neutrons have the same magnitude of angular momentum which can not be increased or decreased. Only their spin axis, the direction of their angular momentum can be changed.

When protons and neutrons combine to form a nucleus, they combine in pairs with opposite spin directions. In a nucleus with an even number of protons, this alignment of the same angular momentum in opposite directions would cancel out each other resulting in no net spin. However, a nucleus with an odd number of protons would have a net spin in one direction.

Almost all elements in the periodic table have an isotope with an odd number of protons which possess a nonzero nuclear spin like ^{1}H, ^{13}C, ^{19}F, ^{23}Na or ^{31}P. As it is much more abundant in the human body than any other, the most important nucleus

for MRI is Hydrogen (H) with only one proton as its nucleus. Due to this fact only H will be considered as the nucleus of choice in the following sections.

3.2.2 Precession

Related to the spin of the proton is a magnetic dipole moment as the H nucleus behaves like a magnet with its spin axis parallel to a north-south axis. When this proton is placed in a static magnetic field, due to the proton's magnetic dipole moment, the static field would exert a torque on the proton which could result in the rotation of the dipole into alignment with the field. But since the proton also has angular momentum, this alignment can not happen immediately and causes the spin axis of the proton to precess around the field axis rather than getting in alignment with it.

The frequency of the precession of a proton in a magnetic field is the resonant frequency of NMR, which is also called the Larmor frequency. The Larmor equation provides the frequency of the precession for that proton with respect to the strength of the magnetic field.

$$\omega_0 = \gamma B_0 \tag{3.1}$$

In the Larmor equation ω_0 is the angular velocity of precession, γ is the gyromagnetic ratio (MHz/T) and B_0 is the strength of the external magnetic field in Tesla (T). As can be seen from the equation, the angular velocity and so the precession frequency is directly proportional to the strength of the magnetic field which applies the torque on the proton. This equation is the fundamental basis of MRI, which uses small manipulations of the resonant frequency to map the location of the NMR signal.

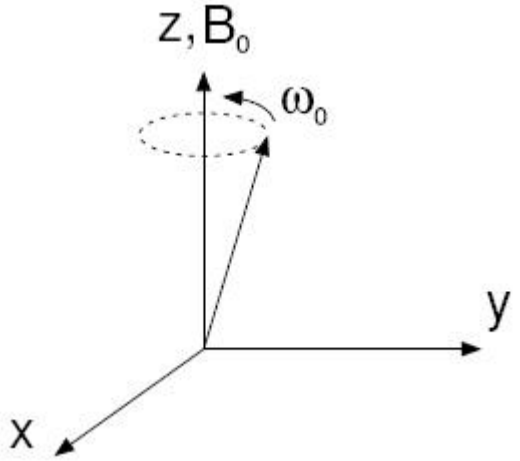

Figure 3.1 The precession around an external magnetic field B_0, at precession frequency ω_0.

The gyromagnetic ratio is a constant different for each nucleus. According to Table 3.1 and the Larmor equation, the precession frequency of H would be 42.58 MHz at 1 T, 63.87 MHz at 1.5 T, and 127.74 MHz at 3 T.

Table 3.1
Gyromagnetic ratios of some nuclei of biological interest.

Nucleus	Gyromagnetic Ratio (MHz/T)
^{1}H	42.58
^{13}C	10.71
^{19}F	40.08
^{23}Na	11.27
^{31}P	17.25

3.2.3 Relaxation

Relaxation is another important process that affects the orientation of the proton's spin. The precession of the dipole around the magnetic field gradually finishes with its alignment with the magnetic field. The time constant for this longitudinal

relaxation process is called T_1 and several times longer than T_1 the dipole essentially aligns with the magnetic field B_0.

When a dipole is aligned with B_0 it is at its lowest energy state, contrary to this, it is at its highest energy state when it is aligned opposite to B_0. With the dipole changing its initial position at any angle to align with B_0, it has to lose its orientational magnetic energy as a form of another energy, due to energy equilibration. This loss is partly dissipated as heat due to random thermal motions of the molecules. The time necessary for this equilibration depends on how tightly coupled the random thermal motions are to the orientation of the dipole. For H molecule in water, this coupling is very weak resulting in a long T_1.

3.2.4 The Radio Frequency Pulse

When a collection of magnetic dipoles such as a sample of water is placed in a magnetic field, the oxygen nucleus would have neither net angular momentum nor a net magnetic moment as it contains an even number of protons and neutrons. On the other hand, the H nuclei with one proton will begin to precess around the field. At equilibrium, the difference between the number of spins aligned with the field and opposed to the field results in a weak equilibrium magnetization, M_0, aligned with the field. The magnitude of this equilibrium magnetization is directly proportional to the local proton density.

The local equilibrium magnetization can not be directly observed since its magnitude is very much weaker than the external field B_0. However tipping over all of the dipoles, which contribute to M_0 by a degree -say 90°- to the transverse plane, would let all of them to precess around the field at the same rate. This would also mean that M_0 to tip over 90°, and results in a measurable, transient signal. This tipping of magnetization is accomplished by the radio frequency (RF) pulse originating from a

transmitting coil.

The oscillating RF current in the transmitting coil, creates an oscillating magnetic field B_1 perpendicular to B_0. Although B_1 is much smaller than B_0, the vector sum of those affects the magnetic field and the net magnetization begins to slightly wobble around the B_0 direction. M_0 also begins to follow this wobbling. If the RF frequency matches the precession frequency of the sample, a resonance phenomenon occurs resulting in the dipoles to absorb energy from the RF pulse. With each precessional rotation, M_0 goes farther away from B_0 until the RF pulse is stopped.

So the net effect of the RF pulse is to tip M_0 from B_0 by an angle, named the flip angle. The flip angle can be increased either by increasing the amplitude of B_1 generated by the RF pulse, or by leaving B_1 on for a longer period of time.

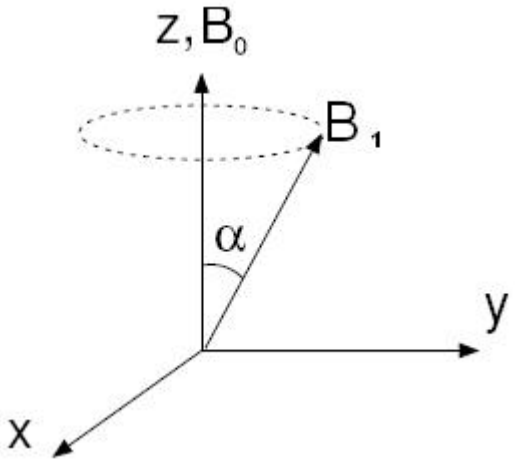

Figure 3.2 Magnetization vector flipped away from B_0, with flip angle α.

3.2.5 The Free Induction Decay Signal

With the help of the RF pulse, the equilibrium magnetization M_0 was taken away from B_0 with a flip angle α. This precessing macroscopic magnetization will produce a magnetic field changing with time which in turn would induce a current in

a nearby receiving coil. This current is actually the measured NMR signal which is proportional to the magnitude of the precessing magnetization. The detected signal is called the free induction decay (FID) signal.

When the RF pulse is stopped, the dipoles which summed up to M_0 will begin to dephase. This is because the tiny random fields generated by other dipoles -protons of other H nuclei- effect other dipoles causing them to precess at different speeds. This dephasing increases with time and as a result they no longer add coherently. The net precessing magnetization on the transverse plane then decays away exponentially, and the time constant for this decay is called T_2. As the transverse magnetization decays, the longitudinal magnetization along B_0 slowly reforms, so that after many T_1 times, the M_0 realigns with B_0.

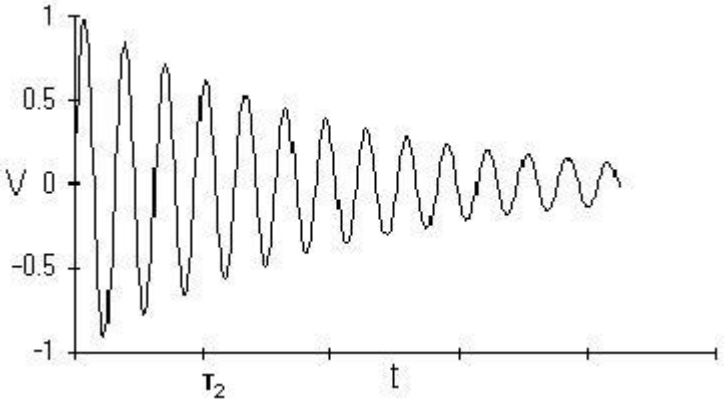

Figure 3.3 The voltage measurement of a detector coil. The signal decays with time constant T_2 in a perfectly homogenous magnetic field.

However, if another RF pulse is applied before M_0 realigns with B0, the longitudinal magnetization will be less than M_0. When this smaller magnetization is tipped over, the magnitude of the transverse magnetization will be smaller resulting in the detection of a smaller NMR signal in the receiving coil. Once again the longitudinal magnetization will grow from zero, but if another RF pulse is applied in the same interval, another FID will be created.

If the RF pulse is sent in same intervals -the repetition time (TR)-, and if the flip angle is 90 degrees, each time the longitudinal magnetization will return to zero after same amount of recovery. As the recovery of the longitudinal magnetization is the same with each interval, the magnitude of the transverse magnetization will also be the same. This will result in inducing the same NMR signal in the receiving coil for all measurements made after the second RF pulse is sent. This signal, regenerated with each RF pulse, is named as the steady-state signal. Almost all MRI applications involve applying a series of RF pulses with the same TR thus resulting in the measurement of the steady-state signal. It can be concluded that M_0 defines the maximum signal that can be generated unless TR is much longer than T_1.

In the example mentioned above, the steady state was reached after one 90° RF pulse, but for other flip angles, several pulses are necessary to reach the steady state.

3.3 Magnetic Resonance Imaging

3.3.1 Image Contrast in MRI

The MR signal depends on several intrinsic properties of the tissue, such as the proton density which effects the equilibrium magnetization M_0 and like the tissue relaxation times. The generated MR signal also depends on parameters of the pulse sequence used such as the TR. With the combination of many parameters a variety of pulse sequences are available. By adjusting those parameters, it is therefore possible to adjust the sensitivity of the resulting MR signal to different tissue parameters to alter contrast in the image. This flexibility is one of the main aspects which make MRI the imaging method of choice. For example, if the TR is longer than T_1, the local magnetization will not depend on T_1 since the longitudinal magnetization will totally recover between RF pulses. However, if TR is shorter than T_1, an incomplete recovery process will result in the local magnetization to depend strongly on T_1, creating a

T_1-weighted signal and image.

A similar approach also works for T_2-weighted images. Some characteristic tissues in the human brain are the white matter, gray matter and cerebrospinal fluid (CSF), which have approximate values of 70ms, 90ms and 400ms for T_2 relaxation. By delaying the measurement of the generated MR signal echo -the echo time (TE)- for about 110ms, it is possible to bring the CSF signal to the front and produce an image showing the CSF the brightest and the rest of the brain parenchyma darker, creating a T_2-weighted image.

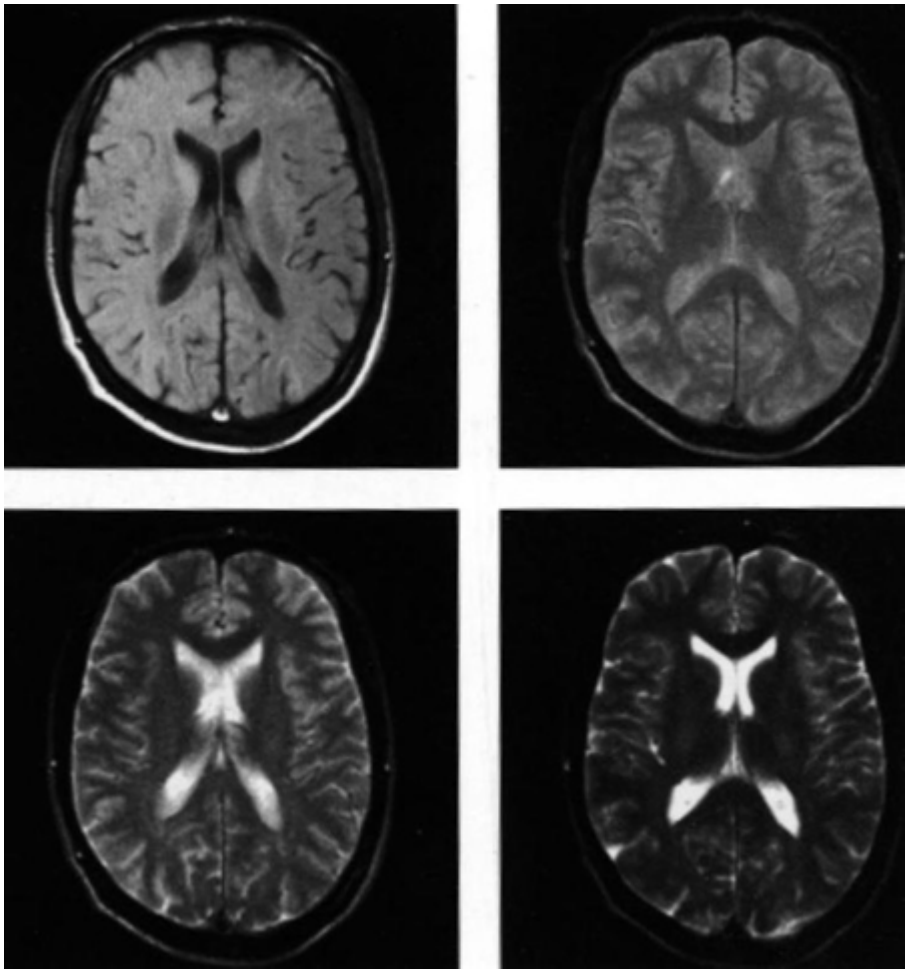

Figure 3.4 The effects of only changing the echo time of a pulse sequence with TR=2500 for all images, TEs=15, 60, 90, 120 from the top left to bottom right.

3.3.2 Radiofrequency Coils

In an MRI scanner, an RF coil is used to detect the MR signal. Depending on which area of the body is investigated, coils of different shapes and sizes are used around the particular area. In brain imaging studies with MRI, a cylindrical shaped coil surrounds the head of the subject. Typically this coil both transmits the RF pulses and receives the NMR signals generated. After a transmission of RF pulses, this coil will receive signals originating from every tissue element in the head which received the RF signal.

To reduce the area of interest, a different type of coil system with separate transmit and receive components are used. This typically consists of a large transmitter coil and a smaller receiver coil which is placed near the part of the head being investigated. This separate receiver coil is called the surface coil and helps in improving signal-to-noise ratio (SNR) since it is nearer to the signal source being received and also provides some volume localization as it receives signals mainly from the part it is imminent to.

3.3.3 Magnetic Field Gradients and Gradient Echoes

The type of volume localization achieved with surface coils is not much delicate for imaging purposes. The spatial localization of the signal received in MRI does not depend on the size or shape of the coils. The actual localization is based on the fundamental relationship of NMR, the Larmor equation (Eq. 3.1) which states that the resonant frequency is directly proportional to the magnetic field at the location of the nucleus.

By applying magnetic field gradients, it is possible to control the local magnetic field and thus the local resonant frequency. In addition to the static magnetic field generated by the MR machine's magnet and the RF pulses generated by the coils,

gradient fields are applied in three dimensions originating from gradient coils in the MR scanner. These gradient fields are used for obtaining spatial information needed for image construction. MRI takes full advantage of this to map locations of received signals and finally produce a meaningful image.

The three gradient coils produce field gradients along three orthogonal directions (x, y, and z). Their combined use results in the application of a field gradient on any direction. For example, an x-gradient produces a magnetic field that is zero at the center of the magnet which becomes more positive at positions in the +x direction and vice versa for the -x direction. Although much weaker, the generated gradient fields add to the main magnetic field B_0, which in turn effects the spins that were previously tipped from B_0 by an RF pulse. This causes the magnetization vectors of the spins at different x locations to precess as different rates, as the dephasing continues the net signal received drops to near zero.

After turning off the gradient, the spins begin to precess at the same rate since B_0 is not under the effect of the gradient pulse, but the phase differences caused by the gradient pulse are carried on. If another gradient pulse with the same amplitude and for the same period is applied with an opposite sign, the rate of spins' precession again changes but they dephase in the other direction this time, rephasing. Finally the effect of the opposite signed gradient pulse, undoes the effects of the first gradient pulse bringing signals arising from different x-positions -for this example- back into phase. This results in the generation of a gradient echo at the end of the second gradient pulse. A gradient echo can also occur with gradient pulses with different amplitudes and durations if the area under the two pulses is the same in opposite directions, which causes the net area under the gradient waveform to be zero.

3.3.4 Localization

In MRI, localization is done in three ways according to the three spatial directions: slice selection, frequency encoding and phase encoding. Generally the slice selection axis is termed as z, the frequency encoding axis as x, and the phase encoding axis as y. However, the actual orientation of this coordinate system in space is arbitrary.

3.3.4.1 Slice Selection. The z gradient (Gz) is typically used for slice selection. A linear gradient field is applied so that the strength of the magnetic field, and consequently the Larmor frequency, increases toward the +z direction and decreases toward the -z direction. When the applied RF pulse's frequency is different from the local resonant frequency, the pulse will have little effect on the local longitudinal magnetization.

Considering the differences in the main magnetic field due to the Gz pulse in the +z and -z directions, a window of spins will be opened in between if an RF pulse with a narrow range of frequencies, $\Delta\omega$, centered on frequency ω_0 is applied. Thus this slice selective RF pulse tips the magnetization to the transverse plane only in the desired slice with spins whose Larmor frequencies are within the $\Delta\omega$ band.

The location of the slice can be selected by varying the center frequency ω_0, of the RF pulse. Increasing the bandwidth of the RF pulse will increase the slice thickness, and vice versa. But if the gradient strength is increased, its effect on resonant frequencies along the z axis will become a steeper function, so the same RF pulse will excite a thinner slice.

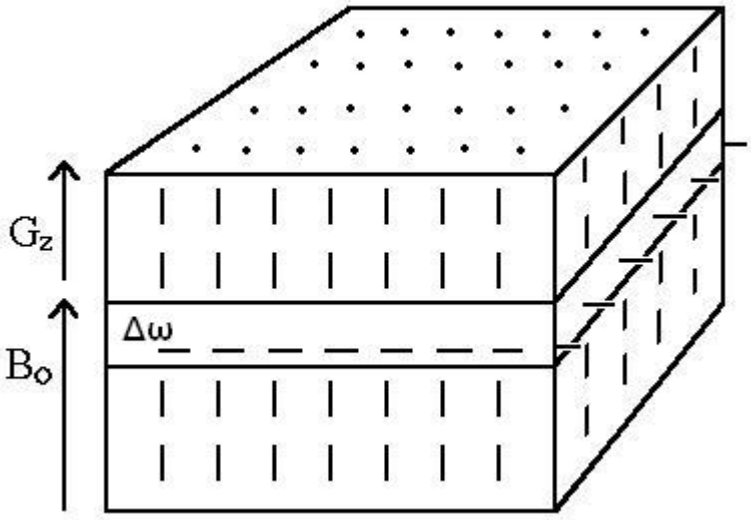

Figure 3.5 Slice selection with the effect of Gz and an RF pulse with a range of frequencies, $\Delta\omega$.

3.3.4.2 Phase Encoding. With the help of slice selection, the effects of the RF pulse are limited to one slice. However, the net signal is still received from all points in the x-y plane. During the interval between the RF pulse and the data acquisition, a phase encoding gradient (Gy) is applied to the currently excited slice along the y axis. As long as Gy is on, the transverse magnetization at different positions in the slice will precess in different rates. This will cause them to dephase. Once the y-gradient is turned off, they will once again begin to precess at the same rate but will also keep their phase differences caused by the Gy. So each local precessing magnetization is now signed with a phase offset proportional to its y-position.

The step is repeated with increasing amplitudes of the y-gradient, with each run of the pulse sequence. This will cause the phase of the magnetization at position y to increase at a rate proportional to Gy.

3.3.4.3 Frequency Encoding. A negative field gradient pulse along the x-axis is turned on after the RF pulse which excites the selected slice. After the negative field gradient pulse, another gradient pulse along the x-axis is turned on, but this time with

the opposite sign (+). Halfway through this second gradient pulse, a gradient echo occurs which the data collection window is centered on. Since the second gradient pulse was turned on during data collection, the precession frequency of the local magnetization varies linearly along the x-axis. This causes the net signal to be transformed from a sum of signals with the same frequency to a sum of signals of a variety of frequencies.

With the help of the Fourier Transform, the measured signal is mathematically transformed. The frequency changes due to Gx, now corresponds to the spatial position of the signal along the x-axis. A similar process takes place to define the signal's origination in the y plane with the Fourier Transform.

3.3.5 The k-Space

When a subject -a tissue sample- is placed in a main magnetic field, the protons of the H nuclei act as magnetic dipoles and by aligning themselves according to the direction of the main field, they create a net longitudinal magnetization. If this magnetization is knocked over to the x-y plane, a local transverse magnetization occurs which can be detected by the receiver coils.

The transverse magnetization has a magnitude depending on local relaxation times and the imaging parameters used. It also has a phase angle defining how much it had precessed up to the detection time. With the application of gradient pulses, the main field goes under a small but effective change. This change either speeds up or slows down the precession depending on the position of the dipoles, resulting in an alteration of the local phase difference. The x-position of a local signal is encoded in the rate of change of the local phase of the signal with time during each data acquisition window. Also the y-position is encoded in the rate of change of the local phase between one phase-encoding step and the next. So, the Gx and Gy pulses both effect the phase of the signal, however they do not interfere with each other.

Using all of the three gradients (Gz, Gx, Gy), allows spatial encoding in three dimensions. Combination of pixels from each slice in all three dimensions creates the volume elements, voxels. By varying the duration and strength of the gradient fields, an entire volume can be pushed into a frequency-phase space, namely the k-space. A time series can be represented as a sum of pure frequencies with different amplitudes. So, a distribution in space can also be represented in terms of amplitudes of different spatial frequencies, k. Thus, the conversion from k-space to an MR image is done by calculation of the two dimensional Fourier Transform for each slice. And with the combination and processing of these slices, a three dimensional image can be formed.

So it can be concluded that MR imaging directly maps the k-space. Thus to enhance or modify the resolution of an MR image, the factors directly effecting the k-space must be modified. And this mainly can be done by modification on the durations, timing and magnitude of x and y gradients in the imaging sequence.

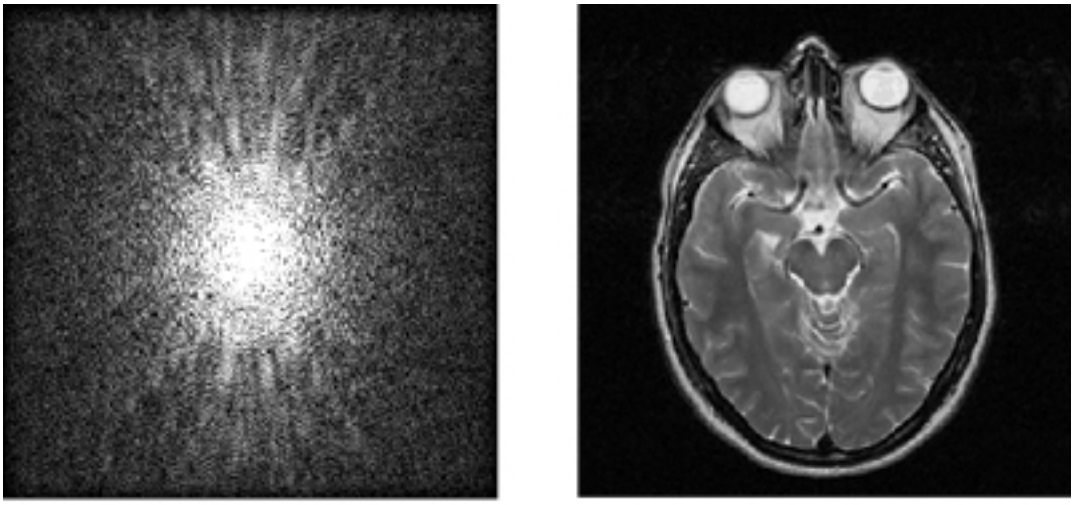

Figure 3.6 a. A k-space data set, with brighter areas indicating high signal intensities. b) MR image generated through merely a 2D inverse Fourier transform of the data set in a.

3.3.6 Pulse Sequences

Image acquisition in MRI depends on several factors like the RF pulses, tissue properties and gradient pulses. The protocols determining the factors that can effect an image acquisition such as pulse timings, durations and strength, are called the pulse sequences.

The difference between pulse sequences, result in getting higher signal intensities from specific tissues with specific relaxation times. Thus allows the imaging system to produce different images with different contrasts of the same phenomenon being investigated. Basically, if the local magnetization depends strongly on the local T_1, the produced image is a T_1 weighted image. Similarly, if the local magnetization mainly depends on the local T_2 value, then the produced image is a T_2 weighted image. Also if a full relaxation of the longitudinal magnetization -which is defined by T_1- is allowed with a long TR and use of a short TE before T_2 comes into play, proton density weighted images can be acquired.

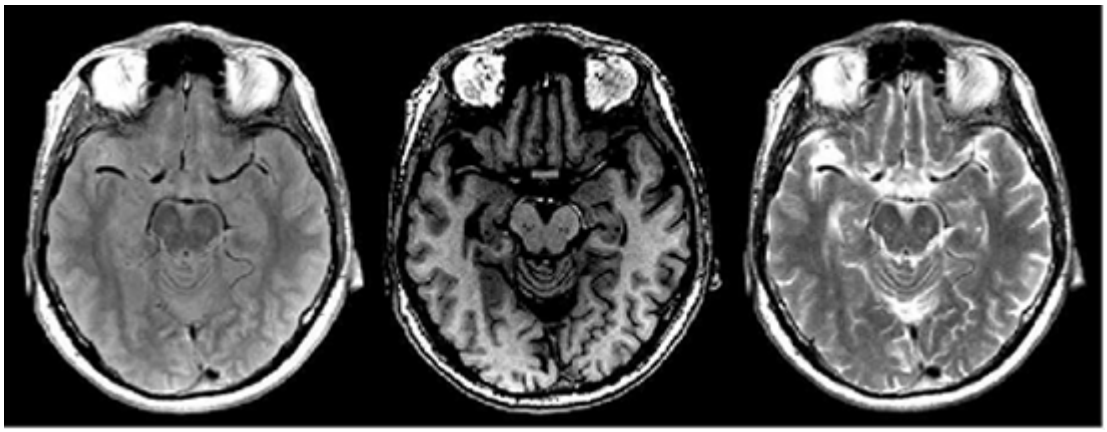

Figure 3.7 Cross sectional brain image. From left to right: proton density weighted, T_1 weighted, T_2 weighted images. Reproduced from [9].

There are mainly 2 main families of pulse sequences in MRI. These are the spin echo pulse sequence and the gradient echo pulse sequences.

3.3.6.1 Spin Echo Pulse Sequence. As mentioned before, the interaction between spins causes dephasing, resulting in the decreasing of the net transverse magnetization over time. This was characterized with a time constant T_2. However there is one more effect in real life situations which causes the net transverse magnetization to decay quicker. This is called the T_2* effect.

No matter how advanced the super conducting magnet used in an MR scanner is, there are still field inhomogeneities in the main field. As the magnetic field changes, this causes spins under the effect of that magnetic field to precess at different rates, so this adds to the dephasing process and thus results in a quicker loss of transverse magnetization. This enhanced decay is described in terms of an apparent transverse relaxation time T_2*.

The inhomogeneities of a magnetic field produced by a magnet are constant, contrary to the random effects which result in T_2 relaxation. So with a cleverly constructed pulse sequence the effects of T_2* relaxation can be accounted for and thus corrected.

The spin echo starts with a 90° RF pulse. With the slice selecting gradient Gz in effect, only the protons in the selected part of the body are excited. At this point the longitudinal magnetization drops to zero and all of the net magnetization vector drops to the transverse plane with individual magnetization vectors in-phase. This creates a signal, however it is too soon to measure it as the signal has to be phase and frequency encoded with Gx and Gy. Also due to the mentioned T_2* effect, some spins precess at slightly different rates. Spins precessing faster than the average rate begin to rotate in one direction and the spins with slower precessing rates rotate in the other direction. As time passes the individual vectors spread into a fan in the transverse plane, reducing the net signal.

Applying a 180° pulse at this point will cause all vectors to rotate through

180°. The spins will keep moving on the same direction, however as they have rotated through 180°, they will realign at some point and form a spin echo at TE. This echo is insensitive to T_2* effects and the 180° pulse is also referred to as the refocusing pulse as this is what it does to the dephased net magnetization vector.

The phase accumulated by a vector caused by the T_2* effect is proportional to the time passed after the first RF pulse. To negate this effect and thus produce a net phase of 0, the same amount of time is needed. So the timing of the 180° pulse is chosen as TE/2.

Image contrast is mainly controlled by the TR and TE manipulations since mostly 90° and 180° flip angles are used with the spin echo sequence. A short TR with a short TE will result in a T_1-weighted image. Using a long TR while keeping the TE short results in a proton density-weighted image. Finally with a long TR and long TE, the produced image will be a T_2-weighted image. Spin echo is the choice of anatomical imaging in the medical field as it eliminates the effects of the T_2* inhomogeneities.

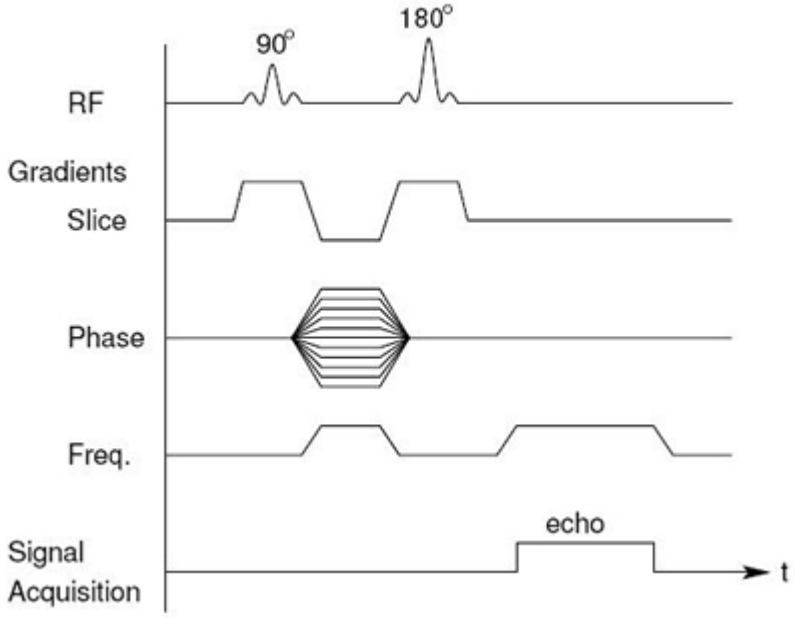

Figure 3.8 Spin echo pulse sequence diagram. Reproduced from [10].

3.3.6.2 Gradient Echo Pulse Sequence. In gradient echo sequences, an RF pulse with a flip angle, α, is used. The flip angle is typically less than 90 degrees. In this type of sequence, a 180° refocusing pulse is not used. Instead, the dephasing protons after the RF pulse are re-phased with the help of gradients of reverse polarity. However this does not eliminate the T_2* effects, thus true T_2 weighted images can not be acquired.

The repetition time and flip angle constitutes an important place in this type of pulse sequences. The combination of these values and intrinsic tissue parameters defines the strength of the signal to be received. The flip angle defines the percentage of the longitudinal magnetization that will be tipped in to the transverse plane with sinα. So a 90° pulse will tip all of the longitudinal magnetization to the transverse plane, generating the strongest signal achievable with the same parameters. Thus, smaller flip angles result in the tipping of a smaller fraction of the longitudinal magnetization. This, generates a weaker signal in the transverse plane, however it also reduces the time in which the longitudinal magnetization fully recovers. As a result the sensitivity of the resulting signal to differences in T_1 is reduced, and also provides a faster pulse sequence over classical spin echo techniques.

It is possible to acquire a T_1 weighted image with a short TR and a large flip angle, whereas the combination of a short TR and a smaller flip angle results in a proton density-weighted image. A small flip angle used with a longer TR and TE will produce T_2*-weighted images. But with modern magnets, such images have similar contrasts to spin echo T_2-weighted images, so they can be called gradient echo T_2-weighted images as well.

With the combination of many parameters and with many variations, it is possible to prepare many different pulse sequences for specific tasks. For example Echo Planar Imaging (EPI) technique does not require repeated RF pulses as gradients are used to cover the whole k-space. For this reason it is pretty fast and this makes the

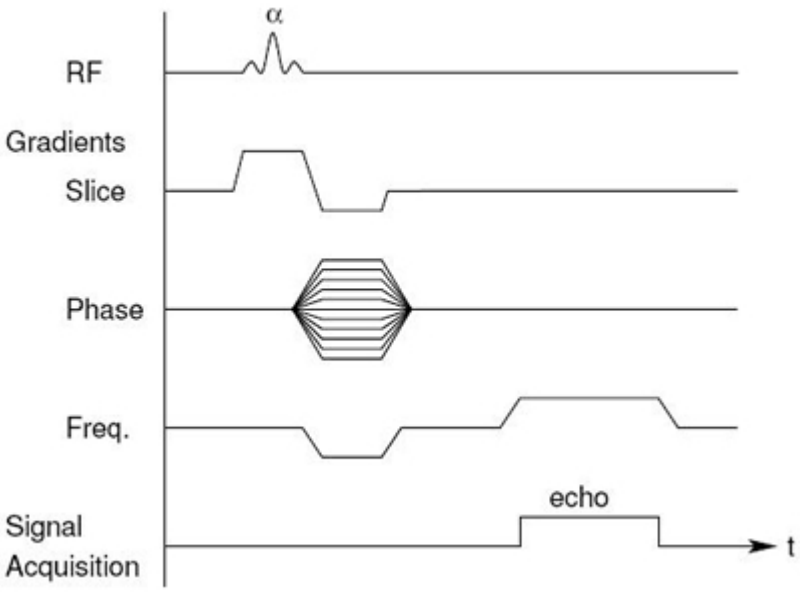

Figure 3.9 Gradient echo pulse sequence diagram. Reproduced from [10].

GRE-EPI pulse sequence a useful tool in acquiring BOLD fMRI images. Also the spin echo EPI is another pulse sequence used in fMRI studies, which is particularly useful in fMRI studies at inhomogeneous areas such as the air/tissue interfaces. This versatility and flexibility makes MRI even more powerful.

4. BLOOD OXYGEN LEVEL DEPENDENT fMRI

4.1 Brain Energy Metabolism

Using electrodes placed on subjects' scalps provides information about the electrical events taking place within the brain. With this information, the location of some sources of those activities may be estimated; however it is not good enough to create a detailed map of the activation patterns. Placing the electrodes directly in the brain could improve the results, but its invasiveness makes it pretty useless in human studies. So instead of directly tracking neural activity, localizing the metabolic activity which fallows neural activity is a more feasible approach in understanding the functional organization of the human brain. This approach is thus followed in the most active neuroimaging techniques used today, which are mainly the PET and fMRI, the latter being the newer but also the more actively investigated one.

Brain generates around 11W/kg of heat as a consequence of its activities [15]. To support these activities, a continuous supply of blood which carries glucose and oxygen is required. The average human heart pumps 3 to 6 liters of blood per minute, and brain receives approximately 15% of that -around 700ml/min. Considering the ratio of the human brain weight to the total body weight being about 1 to 50, the importance of the brain can once again be seen easily.

Neurons, responsible for neural activity have an electric potential difference across their cell membranes mainly depending on sodium and potassium levels. They generate action potentials which is a transient disturbance of their membrane potentials, the rapid depolarization of the membrane. The action potential runs down the axon and reaches a synapse, a junction with another neuron. When the action potential reaches a synapse, the membrane permeability to calcium decreases, resulting in the

inflow of Ca^{++} to the presynaptic terminal. The increase of Ca^{++} in the cell results in the release of neurotransmitters to the synaptic gap. Glutamate is a common example for excitatory, and gamma-aminobutyric acid (GABA) is one example for inhibitory neurotransmitters. The neurotransmitter binds to the receptors of the postsynaptic terminal. This connection either causes the next neuron to get closer or to inhibit the firing of its own action potential depending on the type of the synapse.

Either way the signal was passed from one neuron to another, starting with the generation of an action potential, release of a neurotransmitter and its binding to the postsynaptic receptors, altering the postsynaptic potential. The process mentioned so far does not actually require a source of energy. However, returning the neurons to their prior states in terms of ionic concentrations and the retraction of the released neurotransmitters requires energy. Also keeping the intracellular and extracellular ion concentrations in such a way that the neuron is kept ready to fire a new action potential needs energy.

In biological systems, the free energy is stored in three phosporylated forms of adenosine. These are adenosine triphosphate (ATP), adenosine diphosphate (ADP) and adenosine monophosphate (AMP) [58]. The conversion of ATP to ADP releases the energy that is needed for the processes mentioned before. For example, with the utilization of one ATP molecule, the Na/K pump in neurons can transport 3 sodium ions out and 2 potassium ions into the cell to maintain its membrane potential. This process is pretty continuous as Na constantly leaks into the cell even at the resting stage. The pumping out of the excess Ca at the presynaptic terminal can be another example that requires the consumption of ATP. For each ATP molecule consumed, one calcium ion is transported out of the cell. Also, transporting 3 sodium ions into the cell in exchange of 1 calcium ion transported out of the cell is another way of getting rid of excess calcium [59]. This exchange does not directly require the utilization of ATP, however sodium excess is not also wanted in the cell so it is then transported out with the Na/K pump using 1 ATP molecule.

Conversion of ADP back to ATP requires the metabolism of glucose and oxygen which are provided via the continuous flow of blood to the brain. This metabolism occurs in two stages; glycolysis and the citric acid (TCA) cycle. Glycolysis is an anaerobic process which does not require oxygen. It starts with the uptake of glucose from the blood and ends with the breakdown of one glucose molecule into two pyruvate molecules and the net production of 2 ATP. The healthy brain requires more energy so the pyruvate molecules are destined for the TCA cycle, the aerobic part of glucose utilization. The TCA cycle takes place in the mitochondria, consists of many steps and the involvement of different enzymes finally produces 36 ATP molecules ready to be used. So the total metabolism of glucose with oxygen produces 38 ATP. Carbon dioxide and water are also byproducts of the TCA cycle which are cleared from the tissue via blood flow.

In the healthy human brain, almost all of the pyruvate molecules produced after glycolysis enters the TCA cycle. However, if they are not further metabolized by the TCA cycle, they are reversibly converted to two lactate molecules. Lactate was thought to be formed in abnormal situations such as hypoxia. But the current view is that lactate is formed during most neuronal activation, without apparent oxygen deficiency [60].

The glucose delivered by the blood flow passes into the interstitial space from capillaries via facilitated diffusion. Only around 30% or less of the glucose in the capillaries are extracted from the blood [61]. However, about half of the glucose diffuses back to the blood stream [62], without finding the chance to be metabolized. So only around 15% of glucose delivered via the blood is used. Since this is enough to keep the brain healthy, it can be concluded that glucose is delivered much more than it is needed at rest.

Deoxyglucose (DG), is an analog of glucose with only one oxygen atom missing. It can go under an incomplete glycolysis in the cell. As it is not completely metabolized,

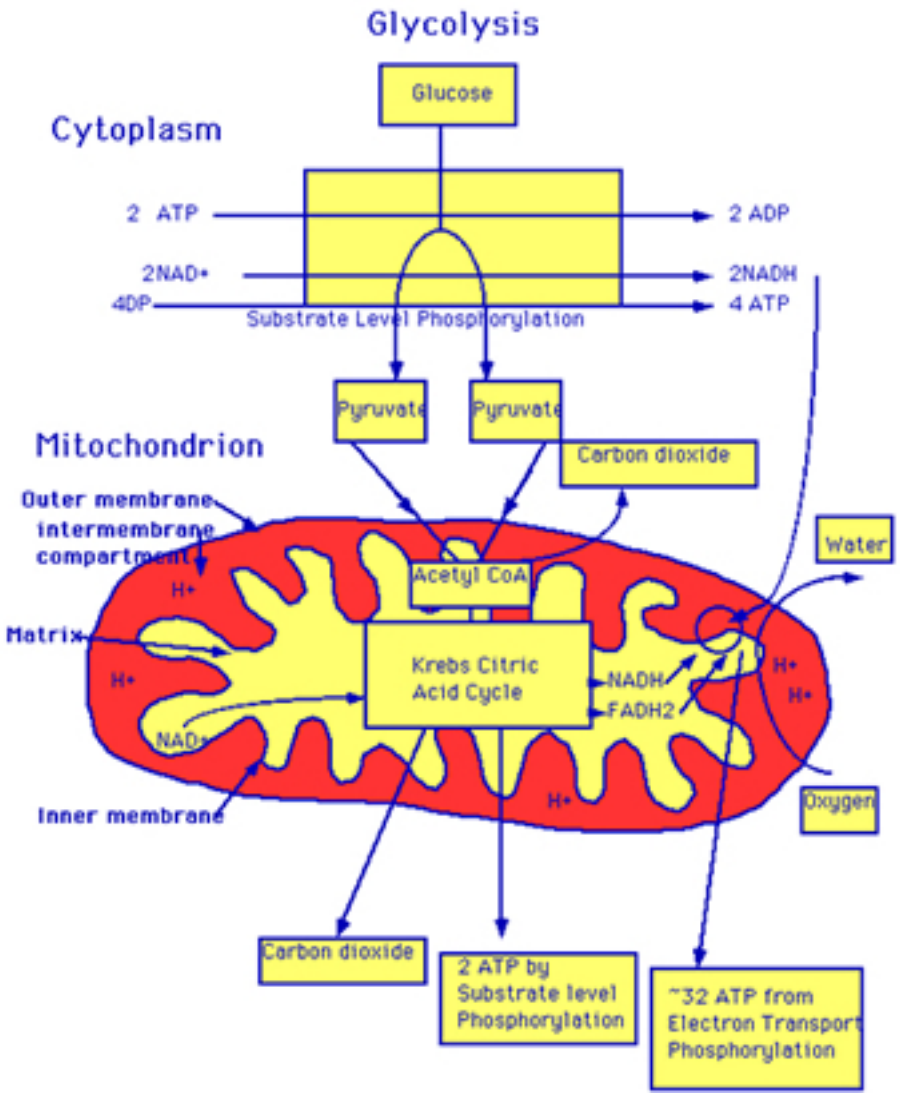

Figure 4.1 Schematic diagram of the major steps of glycolysis and the citric acid cycle. Glycolysis results in the net production of 2 ATP, and TCA results in the production of an additional 36 ATP. The byproducts of the TCA cycle -water and carbon dioxide- are removed from the tissue via blood flow. Reproduced from [11].

and since its clearance from the tissue is slow, it accumulates in the tissue. The development of the DG technique [63, 64] and marking the DG with a radiotracer made it possible to map the pattern of glucose metabolism in the animal brain. Adaptation of the technique to PET with FDG made it possible to study the cerebral metabolic rate of glucose (CMRGlc) in humans.

Over the years, several animal studies have been conducted showing that there is a relationship between local functional activity and local glucose metabolism in the animal brain [65, 66, 67]. Following those, human studies with FDG and PET [68]also showed close correspondence. Furthermore, high-resolution studies of the exact location of increased CMRGlc with increased activation, point to areas of dense synaptic connections having the largest increase in CMRGlc rather than neurons' bodies.

In those studies, areas with high CMRGlc also contain many astrocytes. Astrocytes are part of a group of cells called glial cells or neuroglia, which surround and protect neurons. Other types of glial cells are the microglias which act as the macrophages of the brain and the oligodendrocytes that support and increase conductivity of neurons by surrounding them. Astrocytes are located around the brain capillaries, providing a possible buffer between the vessels and neurons. So glucose can be taken up from blood via astrocytes and passed down to the neurons. However a recent hypothesis suggests that astrocytes not only takes up the glucose, but also preferentially conduct the anaerobic part of glucose metabolism stimulated by neurotransmitters released by the neurons. This results in the release of lactate via an astrocyte-neuron lactate shuttle, which is then taken up by neurons, converted to pyruvate and goes under TCA [47, 69, 60].

To further couple the neural activity to CMRGlc this example can be given: One glutamate is released at a synapse by a neuron following an action potential. An astrocyte takes up the glutamate, converts it to glutamine. This causes the astrocyte to consume 2 ATP, which is the exact amount of ATP produced by glycolysis which

in turn was stimulated by the release of the glutamate. The astrocyte releases the glutamine back to the extracellular space with the 2 lactate molecules produced with glycolysis, which is taken up by a neuron.

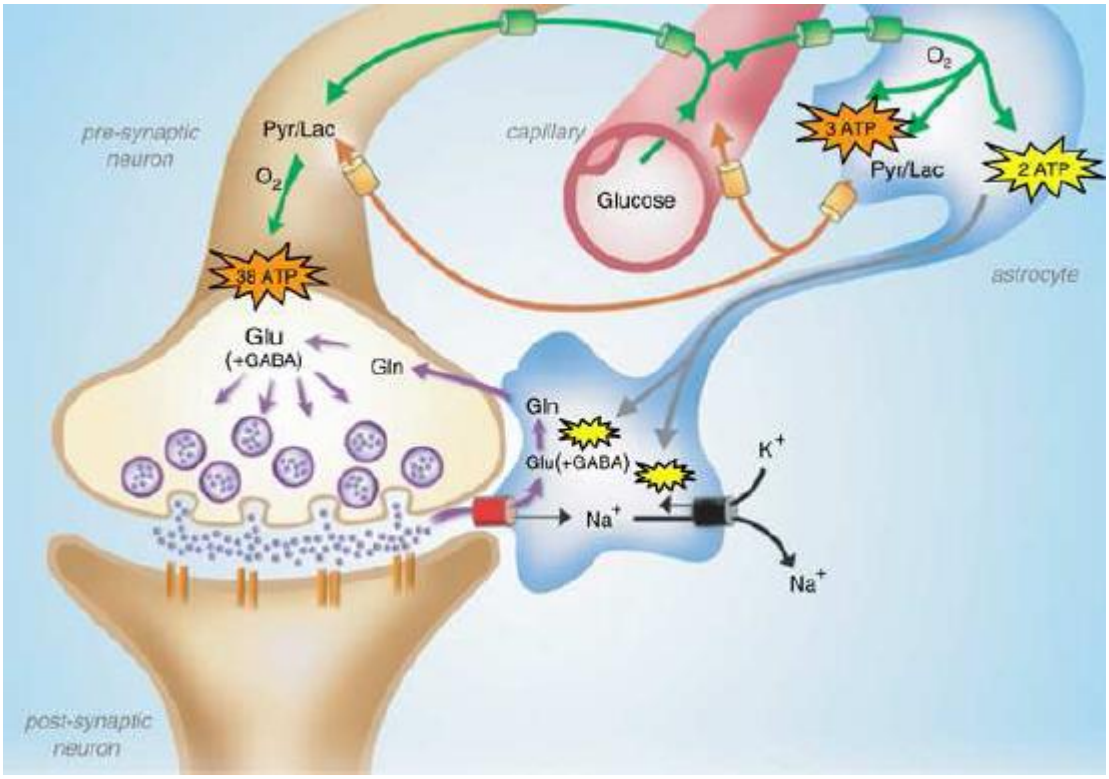

Figure 4.2 An illustration of astrocyte-neuron lactate shuttle. Reproduced from [12].

4.2 Coupling of Brain Energy Metabolism to Blood Flow

Cerebral blood flow (CBF) supplies the glucose and oxygen necessary for neural activity. It can be defined as the delivery of arterial blood to the capillary beds in a particular mass of tissue. The cerebral blood volume (CBV) is the percentage of the tissue volume occupied by blood vessels. For the brain this is around 4%. Around 5% of this value consists of the arterial volume, and the rest 95% is divided evenly between capillaries and veins [70]. The velocity of blood in the vessels is another important physiological parameter which varies mainly according to the diameters of vessels. In

capillaries, the velocity can drop to 1mm/s in a rather irregular fashion than a constant velocity [71]. This is probably because the red blood cells' diameters are about the same as capillaries and are quite deformable.

CBF does not only provide the supplies necessary for ATP generation, but also carries away the waste products of metabolism, being CO_2, H_2O and heat. Because of this, a local increase in CBF following increased neuronal activity is not a surprise. Measuring the rate of delivery of an agent carried to the tissue by flow is a good approach for estimating CBF. The radioactively labeled microspheres method used in perfusion studies in animals [72], the nitrous oxide technique which helped in determining global blood flow [28] that was discussed earlier, the radioactive inert gas technique relying on the time constant of clearance of a radioactive inert gas such as 13Xe from the tissue to estimate regional CBF [73, 74] the PET $H_2{}^{15}$ bolus injection and the PET $C^{15}O_2$ methods [75, 76] have been important approaches in measuring CBF.

Arterial spin labeling (ASL) used in MRI investigations is also a recent technique to measure CBF, with better temporal and spatial resolution and the advantage of being totally non-invasive. In the ASL technique, arterial water is used as an intrinsic tracer. The blood is typically tagged with an RF inversion pulse prior to the entry of imaged slice. As the tagged blood arrives at the tissue of interest, an exchange occurs with the water molecules in the tissue which have a different magnetization state. Several tag and control -not tagged- images of the slice are acquired, and the constructed average difference map from the difference of those images provides a qualitative flow image [77]. The ASL technique is still under heavy investigation and development, however promising results shows that it will be pretty useful especially in the domain of BOLD fMRI.

Flow, in arterioles and capillaries is controlled by the smooth muscles surrounding them. Contraction of the muscles constricts the vessel reducing the vessel diameter, whereas relaxation of the muscles dilates the vessel thus increasing the vessel diameter.

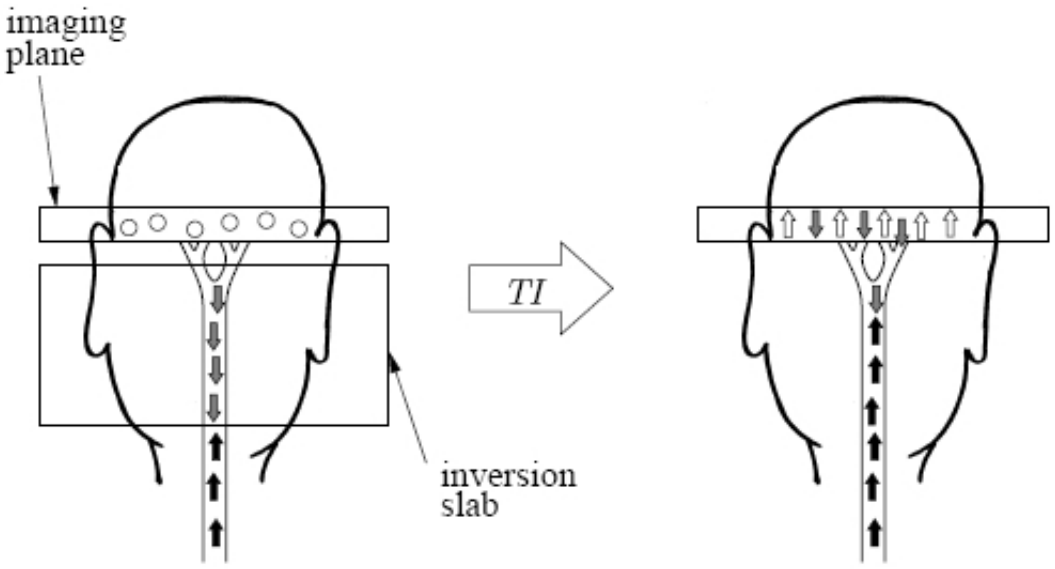

Figure 4.3 Pulsed Arterial Spin Labeling example tagging procedure. The blood's magnetization is inversed before entering the imaging plane. Reproduced from [13].

The actions of those muscles are controlled by local metabolites named vasodilatory agents. So, two mechanisms may control the blood flow via those muscles: the energy use caused by glucose and O_2 metabolism, and the neural signaling to the local vasculature. The vasodilatory agents resulting from metabolic actions are mainly thought to be adenosine, positively charged ions (H^+, K^+) and blood gases (CO_2 and O_2).

CO_2, the byproduct of the TCA cycle affects the blood pH; also it can diffuse into the vessel wall to the muscle. There it reacts with water to form bicarbonate ions and H^+. An increase in the hydrogen ions also causes a decrease in pH. A study conducted in monkeys in which the arterial partial pressure of CO_2 was raised from 40mmHg to 60mmHg almost doubled the global cerebral blood flow [78]. Apparently, the brain is highly sensitive to pH changes, and the increase in CBF may serve to increase the clearance rate of CO_2 and provide some control over pH changes.

Increased K^+ and reduced Ca^{++} concentrations around the cerebral arterioles also causes vasodilatation. Since neural activity causes increased K^+, and reduced

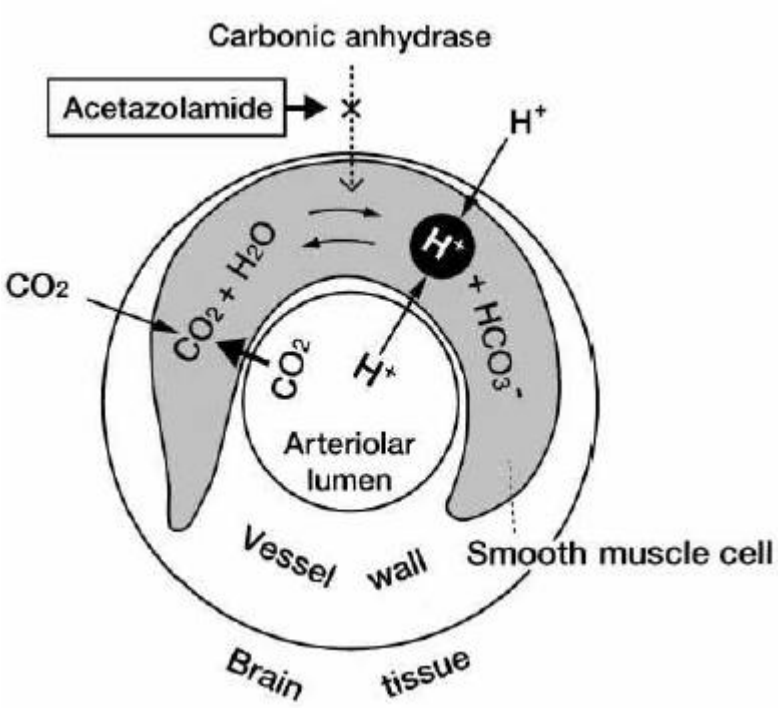

Figure 4.4 Cerebral vasodilator activity of CO_2 and H^+.Reproduced from [14].

Ca^{++} concentrations in the extracellular space, a natural mechanism for increasing CBF with increased neural activity can be established. This is known as the cation hypothesis for CBF regulation [79]. Also the generated energy by the dephosphorylation of ATP causes an increase in adenosine in the cells and extracellular space. Adenosine has a vasodilatory effect [80, 81]. So another mechanism to regulate CBF as a result of neural activities can be seen.

Also nitric oxide (NO) has been found to be important in regulating CBF [82, 83]. It rapidly diffuses through the tissue, is short-lived and is a powerful vasodilator [84]. NO is produced from neurons and astrocytes as a result of glutamate activity that was mentioned before. It is suggested that NO controls the vasodilatory effects of other mediators produced as a result of neural activity. So the control of CBF may include sophisticated relationships between NO and other mediators such as adenosine, CO_2 and K^+.

CBF changes are partly linked to CBV changes, as the change in CBF results from the change in the cerebrovascular resistance. The cerebrovascular resistance is greater in arterioles. Dilation of the arterioles increases CBF, but since arterioles constitute only about the 5% of CBV, the increase in CBV may be much smaller than CBF. Also the distensibility of vessels may cause CBV to increase due to increased CBF causing increased pressure. A study conducted to assess the dynamics of changes in CBV showed that, CBV had longer time constants for reacting and returning to baseline compared to the CBF response [19]. This suggests that the major part of the volume change follows the flow change rather than causing it.

4.3 The Effect of Oxygen Metabolism

A PET study was conducted to measure the change in cerebral metabolic rate of oxygen ($CMRO_2$), which showed a 29% increase in local CBF while only a 5% increase in the local $CMRO_2$ [85]. A future study also demonstrated an uncoupling between CBF and $CMRO_2$, while a CMRGlc measurement was found comparable to CBF. Investigations on the resting distribution of $CMRO_2$ have shown a rather uniform O_2 extraction fraction of about 40% [86]. So if the flow increases by 30% and the O_2 metabolism increases by 5%, then the oxygen extraction fraction (E) drops to about 32%. This is what makes the blood oxygen level dependent signal in fMRI to change. More details on this will be provided on the next section.

The large increase in CMRGlc compared to $CMRO_2$ implies that most of the glucose is consumed via glycolysis and the resulting pyruvate molecules are not passed into the TCA cycle to go under oxidative metabolism requiring oxygen. The unused pyruvate should be reversibly changed to lactate in that case, and this idea was supported with direct measurements of lactate accumulation in humans with the help of spectroscopic NMR studies [87, 88].

The impact of the $CMRO_2$ on the BOLD effect makes it an important aspect in interpreting BOLD responses. This impact was proven with a study design with a sensory activation experiment and a paradigm that altered the CO_2 content of the subject's inhaled air. Both the activation experiment and the increased CO_2, resulted in an increased CBF, however in the increased CO_2 paradigm there was no change in $CMRO_2$. Finally, the results showed that for the same amount of change in CBF, the activation experiment showed a smaller BOLD signal change, caused by increased $CMRO_2$ [89]. Other studies conducted with PET and fMRI [25, 20, 90, 91] not only demonstrated a close relationship between the CBF and $CMRO_2$, but they also suggest that CBF and $CMRO_2$ increase in a graded fashion with increasing neural activity, like in a block design experiment with stimuli presented at different frequencies to the same subject.

An alternative hypothesis is based on the limited oxygen delivery at rest, which causes the imbalance between flow and oxygen metabolism changes as they are tightly coupled to each other [92]. According to this oxygen limitation model, O_2 delivery to the tissue is barrier limited [93]. This limitation which was demonstrated on a canine model [94] sets the extraction fraction be dependent on capillary transit time by explaining that only a fraction of the O_2 delivered to the capillary bed reaches the point of oxidative metabolism. The hypothesis also assumes that an increasing CBF is accomplished by increasing the velocity of capillary blood without capillary recruitment -the opening up of previously collapsed capillaries [95, 96]. Then an increase in CBF causes a decreased capillary transit time a reduced oxygen extraction. So the $CMRO_2$ is proportional to the product of CBF and E. According to this, increased CBF decreases E, so a large amount of CBF increase is necessary to produce a relatively small increase $CMRO_2$.

When this model is applied to a 40% E at rest, the flow must increase by 30% to cause a 5% increase in $CMRO_2$. This is in compliance with the PET study of Fox and Raichle [85]. According to this model, a substantial increase in CMRGlc does not

need to be supported by a large increase in CBF, although the CBF and CMRGlc changes are similar and large. This can be anticipated by considering the blood supply of glucose being much larger then it is utilized at rest (15%), and most of the glucose being consumed in glycolysis rather than full oxidative metabolism.

There is also another hypothesis suggesting that the uncoupling between CBF and $CMRO_2$ is caused by a laggy $CMRO_2$ response compared to CBF. This is demonstrated in bold transients of studies with sustained visual stimuli lasting several minutes [97]. But same transients can also be explained with a CBV change lagging behind the CBF change. The balloon model developed by Buxton et al [98] is a model which tries to explain the dynamic changes in CBV following changes induced by the change in arteriolar resistance by including the mechanical properties of the vessels in calculations.

4.4 The Big Picture

Mainly the CMRGlc, CBF, CBV, $CMRO_2$ and E play important roles for the better understanding of neuronal activations and for the recent functional imaging modalities such as PET and fMRI. However there are still many unanswered questions as to how these entities are related to each other, the coupling and uncoupling between each other and such.

Although, with the light of the studies conducted, it can be suggested that the cerebral blood flow increases substantially, cerebral blood volume increases moderately, the metabolic rate of oxygen increases slightly, the oxygen extraction fraction drops substantially and the local blood velocity in the arterioles, capillaries and venules increases with an accompanying drop in the blood transit time, while the capillary density probably stays about the same [15].

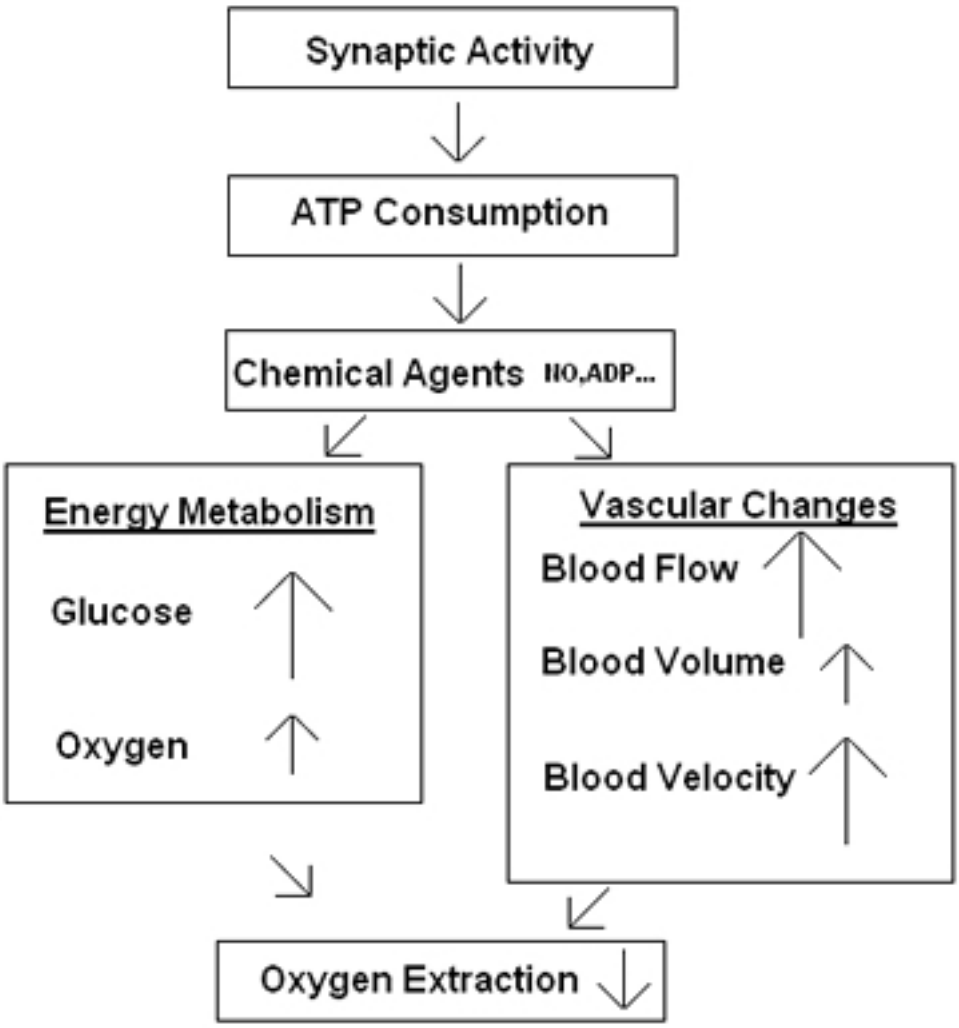

Figure 4.5 Physiological changes accompanying brain activation. Functional neuroimaging is largely based on the metabolism and flow changes in the lower three blocks. The drop in oxygen extraction is the basis of the BOLD signal changes measured with fMRI, but the MR signal is potentially sensitive to blood flow, volume and velocity as well [15].

4.5 Discovery and Basis of the BOLD Signal

Magnetic susceptibility is a measure of the degree to which a material becomes magnetized when placed in a magnetic field. So it is the ability of a substance to produce an internal magnetic field in response to an applied magnetic field. Each substance has different susceptibility values causing them to react differently to the same external magnetic field. As far as BOLD fMRI is concerned, we can classify materials as paramagnetic and diamagnetic.

In paramagnetic materials, there are permanent magnetic moments and when they are placed in an external field their atomic moments line up with the field. Whereas an external magnetic field applied to diamagnetic materials, a weak magnetic moment is induced in the opposite direction of the applied field. When materials of different susceptibility are around each other in the same external field applied, local magnetic field distortions occur. This distortion causes the spins to precess at different rates and dephase quicker adding to the T_2 and T_2* effects.

In studies where brain activation is measured with MRI, external contrast agents such as gadolinium can be used to modify the susceptibility of blood in the test subjects [99]. However, there is an intrinsic physiological agent that alters the blood's magnetic susceptibility, the hemoglobin.

Hemoglobin is a metalloprotein containing iron, which transports O_2 from the lungs to all parts of the body. It is named as oxyhemoglobin (HbO) when it is carrying O_2 molecules, and named deoxyhemoglobin (HbR) when it is free of the O_2 molecules it was carrying. HbR is paramagnetic causing magnetic field distortions, however when O_2 binds to HbR it becomes diamagnetic in the form of HbO.

The fact that HbR is paramagnetic and creates magnetic field gradients inside and around red blood cells was well known [100]. However, it was not until 1990 that the

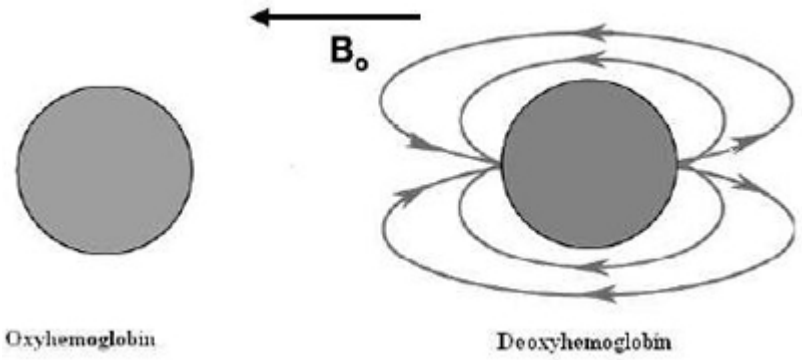

Figure 4.6 Magnetic field distortions due to paramagnetic HbR and diamagnetic HbO. There is no distortion around HbO. However, There is a dipole field distortion in the surroundings of HbR [9].

phenomenon of changes in blood oxygenation following a physiological manipulation produced a measurable effect on MR images [101]. In this animal study conducted with a 9T system, the experimenters modified the levels of O_2 in the subject's breathing air. When 20% O_2 was supplied, the brain image generated many dark lines caused by signal loss, corresponding to the locations of blood vessels. The dark lines disappeared when the subject again breathed 100% O_2. The observed signal loss was interpreted to be a result of the change in the magnetic susceptibility of the blood vessel compared to its surroundings due to an increase in HbR concentration.

Further studies conducted on animals with respiratory challenges also demonstrated that changes in brain oxygenation could be tracked with gradient echo imaging (GRE) [102]. These suggested that natural processes altering the blood oxygenation could also generate a signal detectable with MRI.

In 1992, by Kwong and co-workers reported a study; the demonstration of mapping activation in the human brain using gradient echo MR imaging during visual stimulation and a simple motor task [20]. The study design was to acquire GRE-EPI images, with experiments conducted in 1 minute stimulus period alternating with a 1 minute rest period. As a result the GRE-EPI signal was increased by 3-4% during the visual stimulus and a similar increase was observed in the hand-motor area during

a hand squeezing task. The results of this study and other studies published shortly afterwards [103, 104, 105] marked the beginning of functional human brain mapping based on the BOLD effect.

As discussed earlier, the BOLD signal changes measured with fMRI is a result of the imbalance between blood flow and the metabolism of oxygen. The physical basis of the sensitivity of BOLD MRI signal is that HbR alters the magnetic susceptibility of blood. So the concentration of HbR in a volume tends to reduce the MR signal measured. If flow increases more than O_2 metabolism, less O_2 is extracted from the blood and the venous blood oxygenation therefore increases, also increasing the measured MR signal. This increase is caused by the reduced HbR concentration which shortened the T_2 and T_2* times reducing the MR signal. So the T_2* signal becomes longer with reduced HbR concentration resulting in a stronger signal measured with T_2 and T_2* weighted pulse sequences.

In the last decade, fMRI has been widely used to map the changes in the brain hemodynamics produced by cognitive tasks. However, Due to its signal acquisitions, it has some uncertainties. It is generally believed that significant portion of the signal arises from large veins with additional contribution from capillaries and parenchyma. CBV, CBF and $CMRO_2$ have different effects on BOLD signal [18, 17]. These large veins and physiological activities give rise to uncertainty in localization of fMRI signals and hence make it difficult to understand the underlying physiology of BOLD. In order to suppress and eliminate these uncertainties, several methods have been proposed. Diffusion weighted (DW) EPI [106, 107, 108, 109, 110] and Arterial Spin Labeling (ASL) [111, 112, 113, 114, 115] offers more accurate information about the site of activities and also the signal changes. [9].

4.6 BOLD Transients

The BOLD fMRI does not directly measure neural activity, instead it is a result of combined changes in CBF, CBV and $CMRO_2$ based on metabolic changes following a neural activity. Not any one of those changes can explain the BOLD response alone, but a combination of them, although there are still controversial views as to their coupling and timings can help in explaining the BOLD transients.

For instance, the oxygenation of blood following neural activation depends on the balance of changes in CBF and $CMRO_2$. If both increased at the same level after a neural activity, the oxygen extraction fraction (E) would stay the same causing the level of HbR to stay the same, thus cause no observable changes in the MR. However the increase in CBF is much more than the increase in $CMRO_2$, resulting in a reduced E which in turn causes a more oxygenated venous blood, thus increasing the received MR signal. Again this is not enough to account for all transients observed in BOLD signal.

Since BOLD effect depends on the quantity of HbR in an imaging voxel, it depends on CBV as well. An increase in CBV while E is constant, would increase the total HbR concentration in the area of interest resulting in a reduction of the MR signal, a negative BOLD effect.

Nevertheless, it has been shown that positive BOLD changes correlated with Local Field Potentials (LFP) which suggests that the BOLD signal reflects the synaptic activity, which is directly related to stimulus processing [116]. Within the concept of this correlation, following a neuronal activity, CBF increases dramatically, CBV increases moderately, and $CMRO_2$ increases by a much smaller amount. Therefore, all these physiological activities result in a reduction in the amount of HbR within the tissue so the MR signal increases.

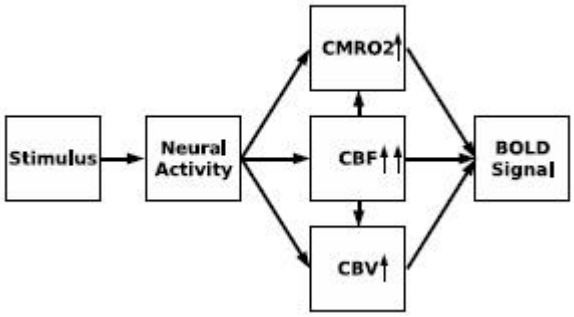

Figure 4.7 The combined changes in $CMRO_2$, CBF and CBV following a neural activity results in the BOLD signal [15].

When the stimuli are presented in a block design like the one in this study, the temporal stimulus pattern is simply a square wave. To a first approximation, the BOLD response in many areas of the brain looks like a delayed and smoothed version of the stimulus pattern [15]. However, a number of transient patterns have been reported to occur at the transitions between rest and active states. These are namely the initial dip, the positive BOLD and the post stimulus undershoot (PSU) [17].

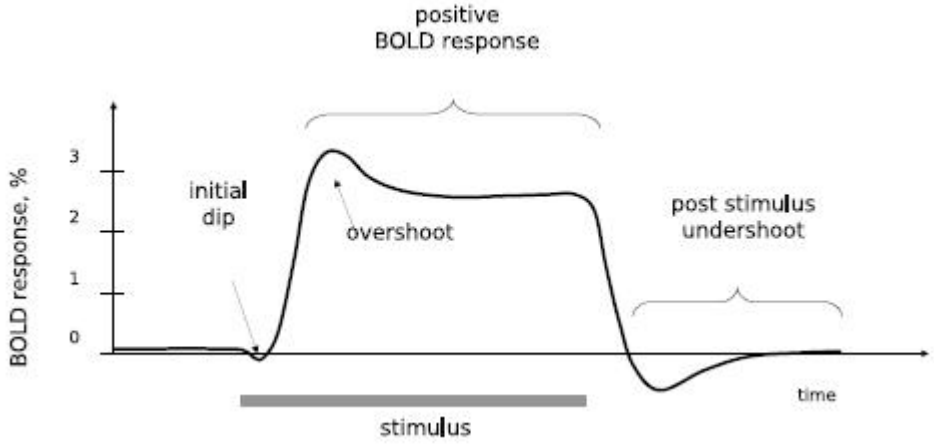

Figure 4.8 An illustration of the BOLD response with the three transients: the initial dip, positive BOLD and the post stimulus undershoot.

4.6.1 The Initial Dip

As the name implies, initial dip is an initial drop of the BOLD signal below the baseline following the beginning of a stimulus. It is potentially accepted as one of the most important aspects of BOLD, while being the most controversial. It was observed in an animal optical intrinsic study (OIS) depending on signals that are sensitive to HbR and HbO [117]. The results showed an increase in HbR peaking about 2 seconds after the stimulus onset, followed by a later decrease of HbR a larger magnitude about 3 times. It was suggested that this fast response is a consequence of a rapid increase in $CMRO_2$ before an increase in CBF begins. As this early change in $CMRO_2$ is better localized to the activated area in the experiment, if true this would mean that the initial dip could provide a much more accurate map of neural activity in fMRI experiments. However, a similar observation of the initial dip could also arise from an initial increase in CBV.

There were speculations as to the origin of the initial dip was an artifact caused by keeping the interval between consequent stimuli short, thus blocking a full recovery of the hemodynamic response [118]. However this idea was proven wrong by a study conducted with longer stimulus intervals [119].

So there are mainly two hypotheses concerning the initial dip. A slight delay of the CBF response compared to the $CMRO_2$ response [120], and an initial increase of CBV following a neural activity [98] (Figure 4.9). The initial dip is still an active area of research so more controversial approaches may arise in the near future.

4.6.2 Positive BOLD

Postive BOLD plateau is the best identified part of the BOLD response. After an increased neural activity, the CBF increases much larger than $CMRO_2$ resulting in

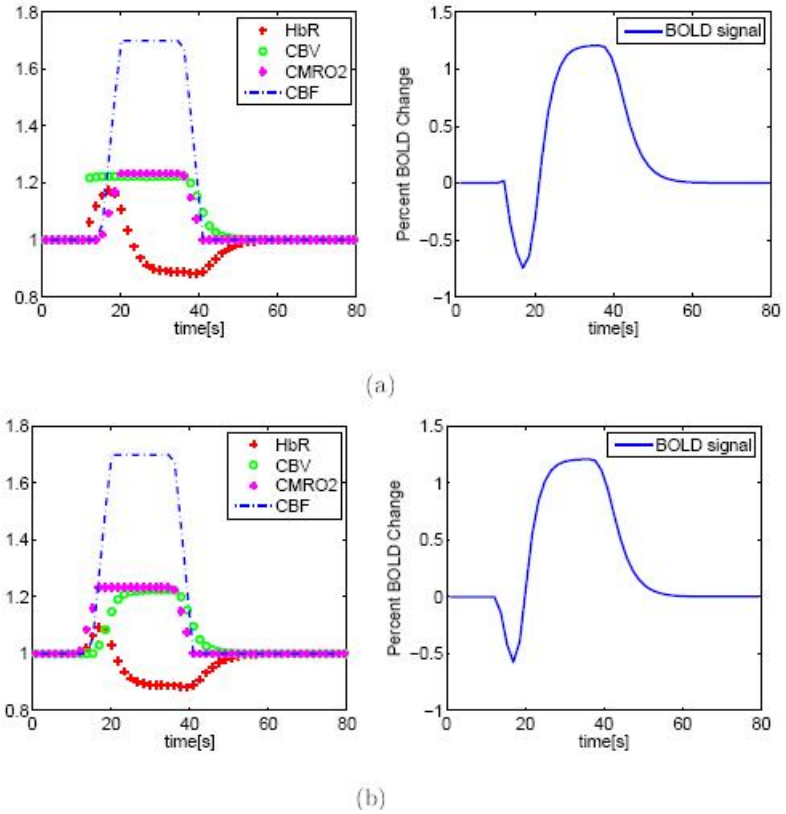

Figure 4.9 (a) CBV based initial dip. (b) $CMRO_2$ based initial dip [9].

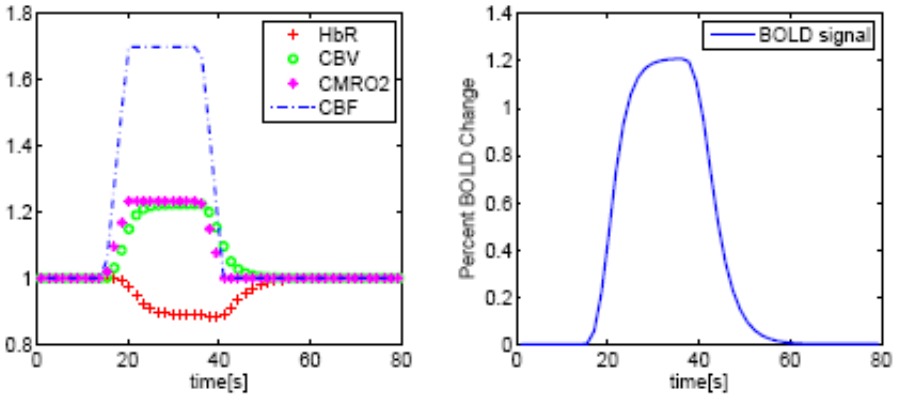

Figure 4.10 An illustration of the postive BOLD transient. The increase in CBF following activation exceeds the increase in $CMRO_2$. This mismatch results in a decreased HbR concentration causing the positive BOLD signal [9].

a decrease of E. As a consequence the HbR concentration drops, generating a positive BOLD signal change [85] (Figure 4.10).

4.6.3 Post Stimulus Undershoot

The origins and the significance of the post stimulus undershoot is another subject of debate since the first papers published on BOLD fMRI [20]. As discussed, the concentration of HbR in the imaged volume is at the heart of the BOLD signal. So a change in the BOLD signal towards negative polarity would mean an increase in the HbR concentration. This idea is supported by optical imaging studies showing an increased HbR concentration with a reduction in HbO concentration following the end of the stimulus [121]. The pattern of a relatively long lasting undershoot is often seen in experiments where the period of resting blocks are the same or greater than stimulus periods [122].

The reason of the increase in HbR could be because of one of the changes, or combined changes of or differences in time courses of the CBV, $CMRO_2$ or CBV. Several studies based on mainly three ideas have been conducted. A temporary fall of CBF under the baseline [123]; a slower return of the $CMRO_2$ to baseline than CBF does [97, 124, 125] and the delayed return of CBV to baseline [108, 126, 17].

For the first hypothesis, if the CBF falls below baseline while $CMRO_2$ holds its position around the baseline, the oxygen extraction would increase. This increase in E, would result as an increase in HbR thus causing the post stimulus undershoot. This hypothesis was supported in several studies [127, 128, 129]. However, other studies found that the post stimulus undershoot was not present in the CBF signal [98, 130]. A study was conducted in 1.5T, in which the subject performed a motor task and viewed a flickering black and white checkerboard for 20 seconds and rested for 100 seconds. An ASL pulse sequence (QUIPSS II) was used to measure flow and BOLD changes

simultaneously in both the visual and motor areas of the brain. Both areas showed a pronounced post stimulus undershoot in the BOLD signal while there was no evidence of an undershoot in flow [131]. However, this does not exclude a CBF undershoot for certain stimuli and baseline states. It has been proposed that a post-stimulus BOLD undershoot can also be caused by a CBF undershoot following reduction of neuronal activity [128] (Figure 4.11b).

According to the second hypothesis, a slower return of the $CMRO_2$ to baseline than CBF does, is the cause of the PSU. So if CBF returns to baseline quicker than $CMRO_2$, the elevated $CMRO_2$ would increase the oxygen extraction thus increasing the HbR concentration. And this causes the BOLD signal to drop under the baseline, and gradually return to baseline as the $CMRO_2$ slowly returns to basleline. Again several studies reported this type of behavior in the hemodynamic responses [97, 132, 133, 134, 125] (Figure 4.11c).

Finally, the delayed return of CBV to baseline is hypothesized to be the reason of the post stimulus undershoot observed in BOLD fMRI studies [98, 19]. In an experiment where a long lasting intravascular contrast agent is used to monitor CBV dynamics and laser doppler flowmetry to measure the CBF was conducted in an animal study. A reasonable return of CBF to baseline, but an elevated CBV with a time lag that matched well with the duration of the post stimulus undershoot was observed in the results of this study. [19]. Furthermore a study was conducted by the same team to address the effects of $CMRO_2$ on PSU, with a variation of the calibrated BOLD technique where the subject inhaled CO_2. The estimated dynamic curve of $CMRO_2$ was observed closely following the CBF curve, with a smaller fractional change [135]. These study results support the idea that $CMRO_2$ is tightly coupled to CBF and that CBV recovery after activation lags behind CBF recovery (Figure 4.11a).

Two similar biomechanical models have been proposed aiming to explain how the post stimulus undershoot can be observed in the BOLD signal, and not present in

flow while CBV is slow to return to baseline [98, 136]. Namely the balloon model by Buxton and the delayed compliance model by Mandeville.

The balloon model treats the capillary bed as a fixed set of pipes assumed to be indispensable. However, post capillary veins are distensible and changes in blood volume all occur on the venous side. The dilation of arterioles, which take up much less of a volume percentage are assumed to be negligible as far as CBV changes are concerned. The vascular bed within a small volume of tissue is then modeled as an expandable venous compartment (balloon) that is fed by the output of the capillary bed. The volume flow rate into the tissue is an assumed function of time that drives the system. The volume flow rate out of the system is assumed to depend primarily on the pressure in the venous compartment. This pressure depends on volume of the balloon [9]. The balloon model is discussed in detail in the book by Richard B. Buxton, "Introduction to functional magnetic resonance imaging - principles & techniques" which I also used as a main reference in writing this thesis.

Functional neuroimaging with BOLD fMRI is promising to become the number one tool in diagnostic radiology and perhaps will be a great help in understanding the working human brain. However, the controversial results and opinions as to its origins and behavior indicates that there is still time before it becomes a golden standard.

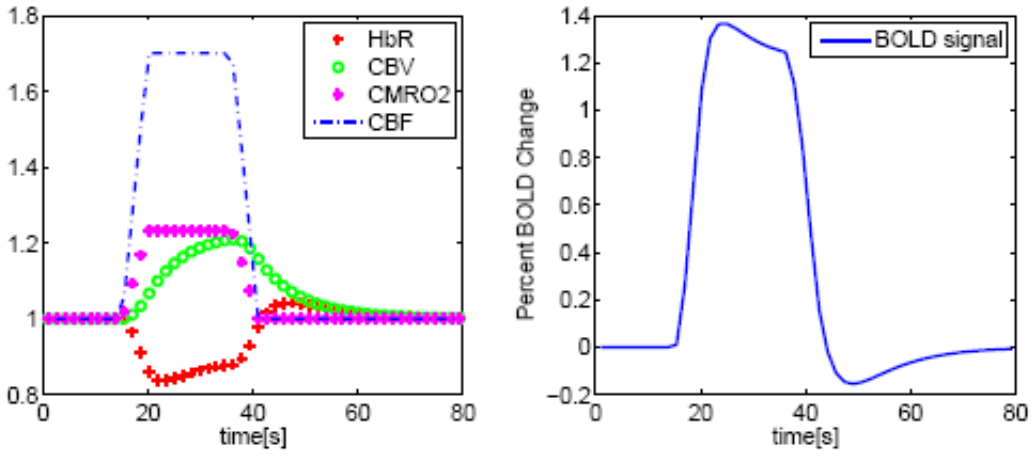

(a)

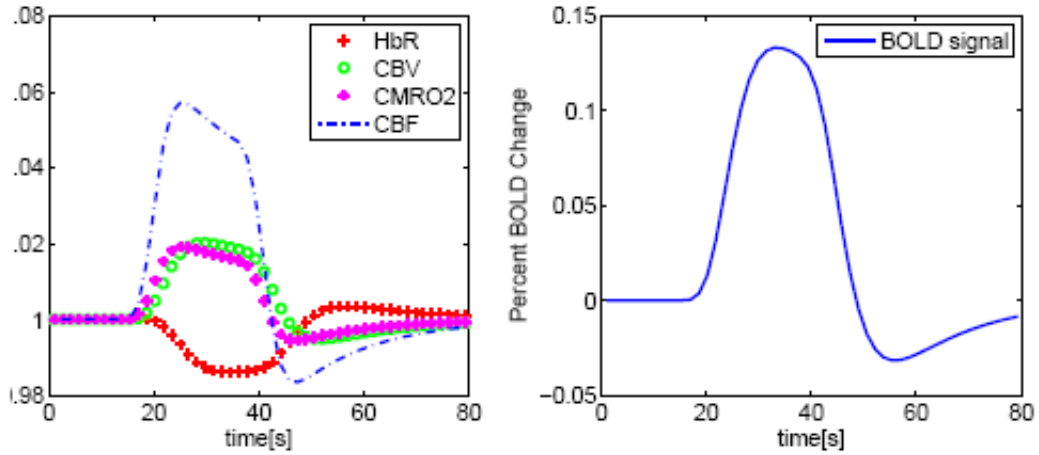

(b)

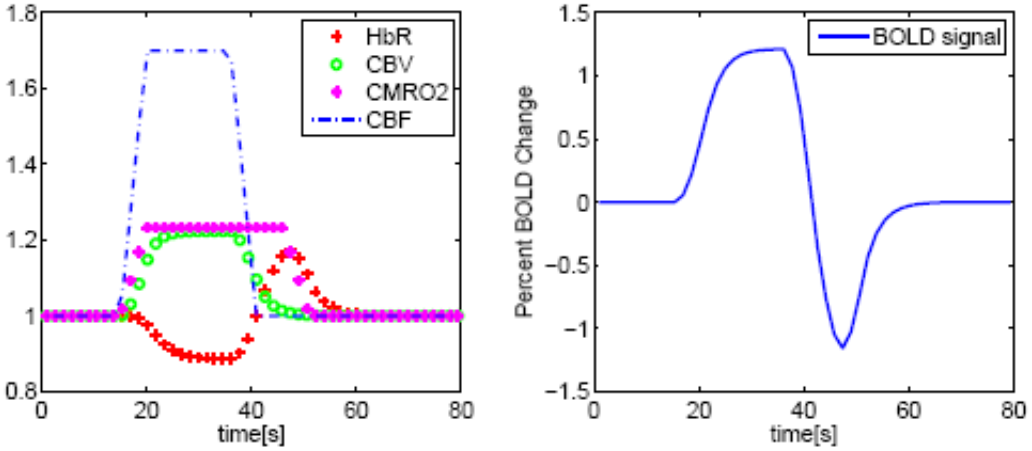

(c)

Figure 4.11 An illustration of post stimulus undershoot due to (a) delayed return of CBV (b) CBF undershoot below the baseline (c) CBF returns to baseline before $CMRO_2$ following stimulus cessation [9].

5. METHODS

5.1 Subject and Study Design

One healthy male subject aged 29 was recruited for the study. A complete description of the study prior to the experiment has been briefed to the subject and his written consent was acquired. The subject lay in supine position, and was told not to close his eyes during both the rest and active periods of each experiment. One static and 11 flash stimuli flickering at frequencies 4, 6, 8, 10, 12, 14, 30, 34, 38, 42 and 46Hz were presented to the patient in the scanner room. The order of the stimuli was generated randomly as static, 46, 6, 14, 12, 42, 34, 10, 4, 38, 8 and finally 30Hz.

Each frequency run begun with a 30 second rest (ie: complete darkness) block, followed by 90 seconds of stimulus, 120 seconds of complete darkness, and a repeat of the 90 seconds stimulus fallowed by another 120 seconds of complete darkness. So the total experiment time for each frequency was 450 seconds. To observe the post stimulus undershoot effect, the rest block was chosen relatively longer than the stimulus block [122]. Also the lights in the scanner room and the MR control room were switched off to avoid any external light viewable by the subject. The protocol timing diagram can be seen in Figure 5.1.

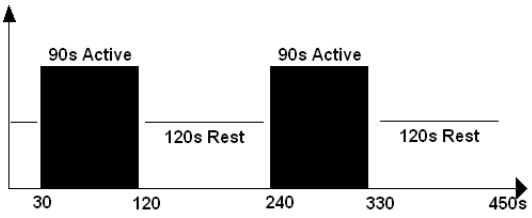

Figure 5.1 Stimulus timing diagram. Each frequency run begins with 30 seconds of rest, followed by a 90s active stimulus then by a 120s rest period. Same stimulus is applied for another 90 seconds and the run for the selected frequency ends with a final 120 seconds of rest period. The subject was told to keep his eyes open at all times, including the rest periods.

The stimulus delivery system's schematic diagram can be seen in Figure 5.2.

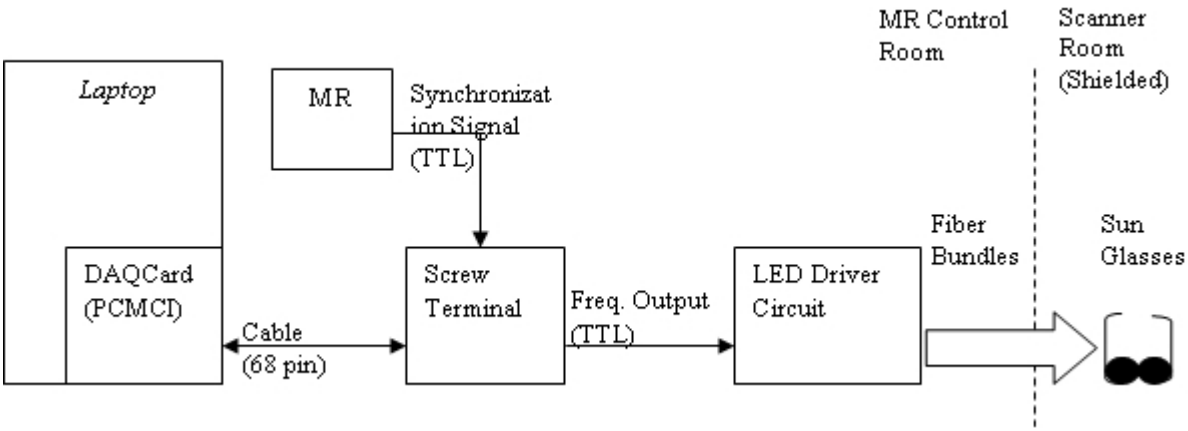

Figure 5.2 The schematic diagram of the stimulus delivery system.

The DAQCard (NI DAQCard-6062E, PCMCI) is used to detect MR synchronization output (60 microseconds width, 5V amplitude, square wave) which rises at the beginning of each TR, to generate the desired frequency output. The DAQCard is connected to a screw terminal (NI SCB-68, Shielded) with a 68 pin cable (NI SC 68-68, 1 m). A stimulus presentation software was coded in Visual C++ language, receiving MR synchronization signals through a digital input line of the DAQCard triggers a function in the software allowing the progress in block design. The method of synchronization, stimulus frequencies and duration of active and rest blocks can be defined through a guided user interface (GUI) as seen in Figure 5.3.

The output of the DAQCard (TTL) is sent to a LED driver circuit (Figure 5.4) in which a 2N 3904 (NPN General Purpose Amplifier) is used as a switch housing 6 parallel SML10CW2KZT-TR LEDs (1000mcd, Ledtronics Inc., Super Cool White, PLCC Surface Mount LED). The LEDs are coupled to fiber bundles (5 pieces, 1mm diameter with plastic closure). The fibers penetrate into the scanner room from a shielded hole between the scanner and control rooms. 4 of the fibers are passed through the glasses of a full black, opaque, plastic sunglass marking the end point for the

delivered stimulus being the eyes of the subject.

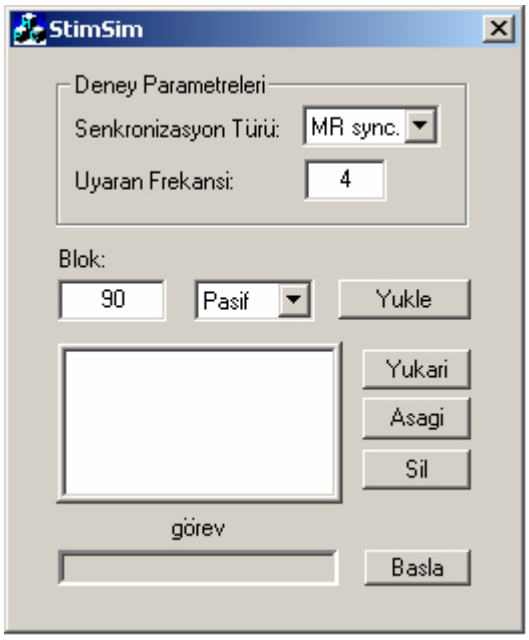

Figure 5.3 Guided user interface (GUI) of the stimulus presentation software.

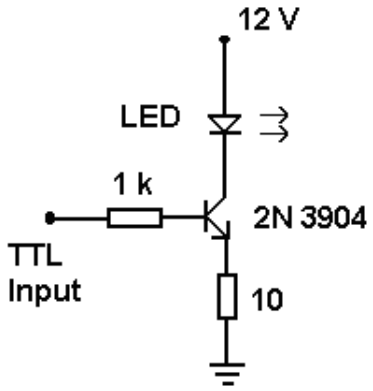

Figure 5.4 The LED driver circuit.

5.2 fMRI Data Acquisition and Analysis

The experiment with fMRI was performed on a Philips 1.5 Tesla MR system using an 8 channel head coil (Sense Head 8, Philips Medical Systems, Eindhoven, Netherlands) at the NPISTANBUL Neuropsychiatry Hospital, Istanbul. Following a

localizer scan, a structural image of the subject was acquired with a standard MPRAGE sequence for future studies. A single shot T_2* weighted gradient echo (GE) echo planar imaging (EPI) sequence was used for BOLD measurements. 32 transverse slices covering the whole brain, over a field of view of 230 x 230 mm with 64 x 64 resolution were acquired with a slice thickness of 4 mm. Other imaging parameters were TR 3000 ms; TE 50 ms and flip angle 90 degrees. Thus, 150 BOLD-based volume images were acquired within each frequency run.

For each measurement of each frequency, all of the volumes were registered to the 5th volume in order to remove motion artifacts by using 3dvolreg function from the AFNI (Analysis of Functional Neuro-Images [137]) program package. First level GLM analysis was carried out using FEAT (FMRI Expert Analysis Tool) Version 5.63, part of FSL (FMRIB's Software Library, www.fmrib.ox.ac.uk/fsl) program package. The following pre-statistical processes were applied: spatial smoothing using a Gaussian kernel of FWHM 5mm; mean-based intensity normalization of all volumes by the same factor; high-pass temporal filtering (Gaussian-weighted least-squares straight line fitting, with sigma=210s). Time-series statistical analysis was carried out using FILM with local autocorrelation correction. This produced a fairly large region of activation within the visual cortex. A fixed-effect group analysis was performed to combine statistical parametric maps of the first level analysis for the subject across all stimulation frequencies. This resulted in a Z-score map of statistically significant stimulus related activity across all stimulation frequencies for the subject. Z (Gaussianised T/F) statistic map was thresholded using clusters determined by $Z>12.5$ and a (corrected) cluster significance threshold of $P=0.05$. This extracted a mask that consisted of a most active cluster including 40 voxels in the visual cortex for each frequency. For each stimulation frequency of the subject, average BOLD signal time course was computed from all activated voxels within the mask. The results were carried to MATLAB (MATLAB 7, The MathWorks Inc., Natick, Massachusetts) software, the BOLD percent change vs image count graphs were acquired by discarding the last 10 images and averaging the two trials (10 images at rest -baseline-, 30 images during stimulus and 30 images at the end

of stimulus), of each frequency. Also the time course of the BOLD signal was averaged across all frequencies for positive BOLD and PSU. The average percentage of PBOLD over 20 images (60 seconds) was calculated 10 images (30 seconds) after the beginning of stimulation. The PSU interval was defined as the 20 images (60 seconds) following stimulus cessation. The percentage changes of the BOLD signal during PBOLD and PSU response periods for each frequency were separately normalized to a maximum change of 1. The resulting plots can be found on the next section.

5.3 Results

The functional map due to visual stimulation from one of the frequencies, overlaid onto the anatomical image, is shown in Figure 5.5.

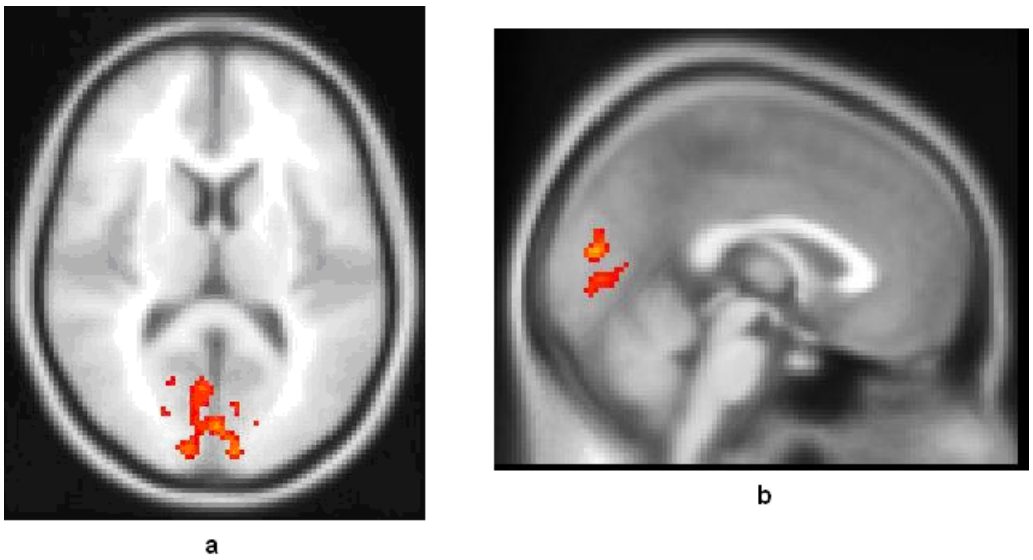

Figure 5.5 The most active voxels for the 6Hz stimulus data is superimposed on top of the subject's structural scan. a: axial view, b: sagittal view. The most activate voxels defined by the mask are primarily located in the primary visual cortex as expected.

All of the flashing stimuli resulted in similar positive BOLD time courses compared to the corresponding static stimulus' positive BOLD time courses. However, following the end of the stimulus, the static stimuli caused no undershoot, while un-

dershoots of varying degrees in all of the flashing stimuli's existed. The recovery of the flashing stimuli BOLD signals to baseline took about 45 seconds (Figure 5.6, Figure 5.7, Figure 5.8).

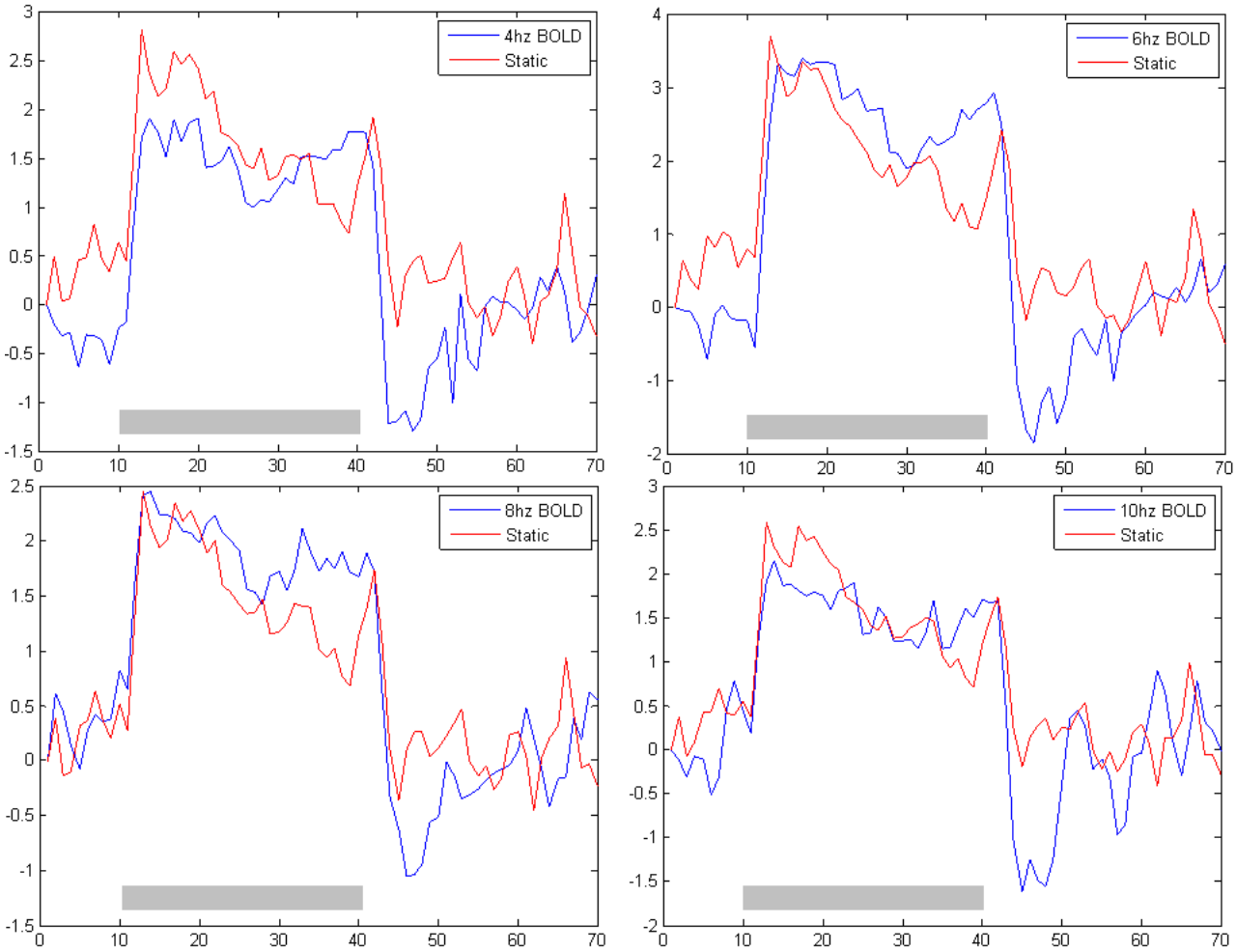

Figure 5.6 Average time courses of BOLD response for flickering stimuli (4, 6, 8, 10Hz) with static stimuli. Similar positive BOLD time courses for the static and flashing stimuli is visible. However only flashing stimuli display a post stimulus undershoot. x-axis: image number (x∗3=seconds) , y-axis: %BOLD change. Gray bar denotes stimulus on time.

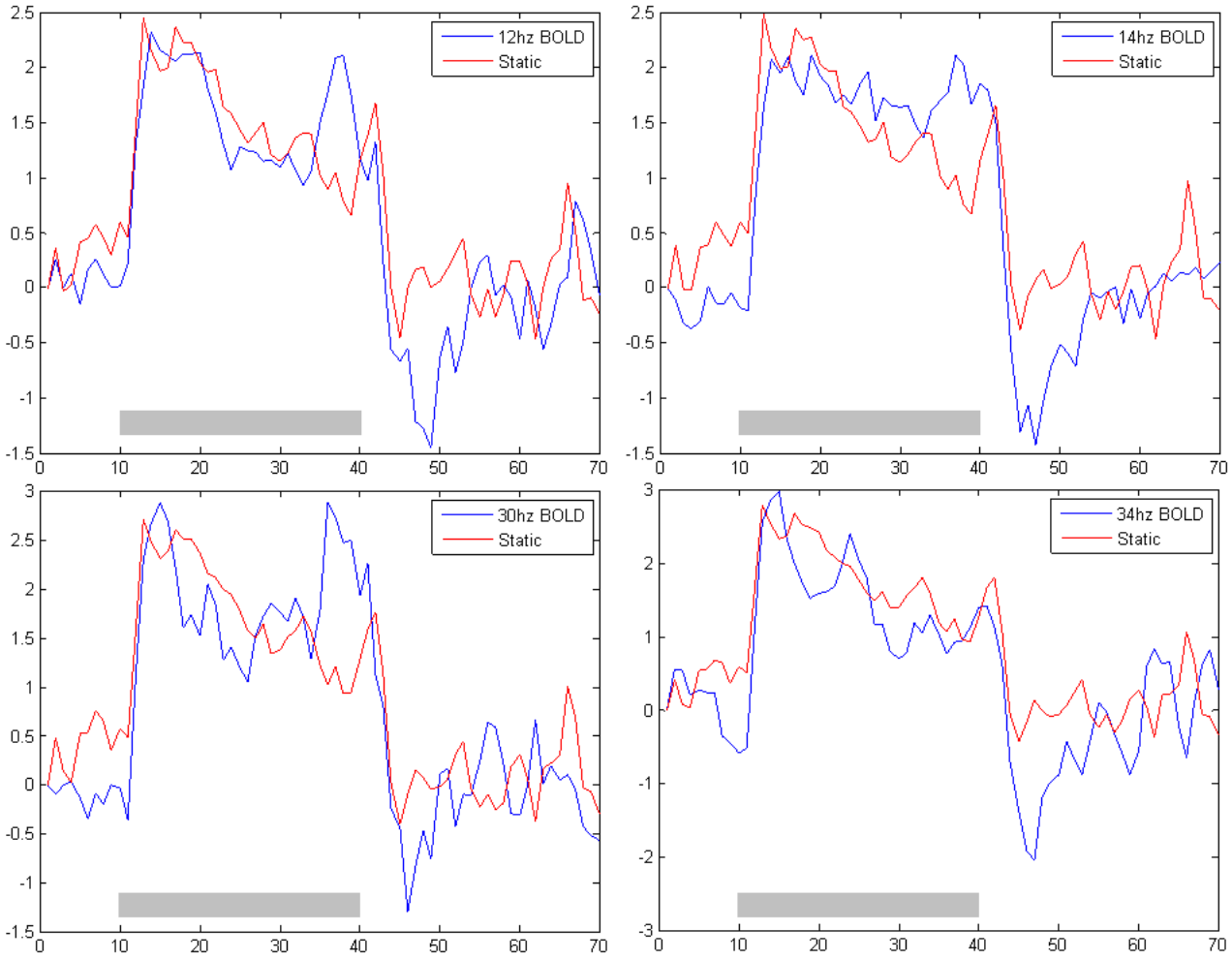

Figure 5.7 Average time courses of BOLD response for flickering stimuli (12, 14, 30, 34Hz) with static stimuli. Similar positive BOLD time courses for the static and flashing stimuli is visible. However only flashing stimuli display a post stimulus undershoot. x-axis: image number (x∗3=seconds) , y-axis: %BOLD change. Gray bar denotes stimulus on time.

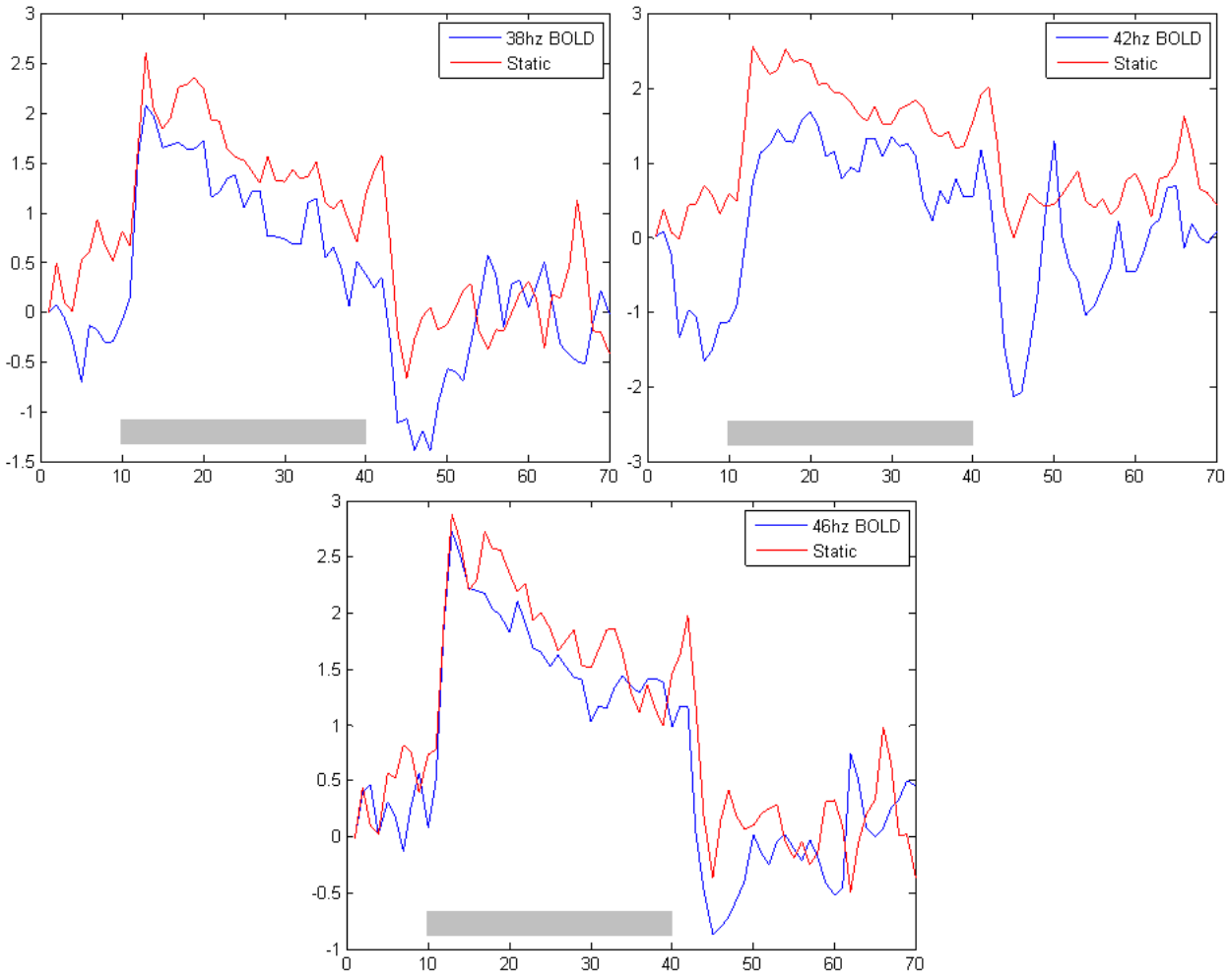

Figure 5.8 Average time courses of BOLD response for flickering stimuli (38, 42, 46Hz) with static stimuli. Similar positive BOLD time courses for the static and flashing stimuli is visible. However only flashing stimuli display a post stimulus undershoot. x-axis: image number (x∗3=seconds) , y-axis: %BOLD change. Gray bar denotes stimulus on time.

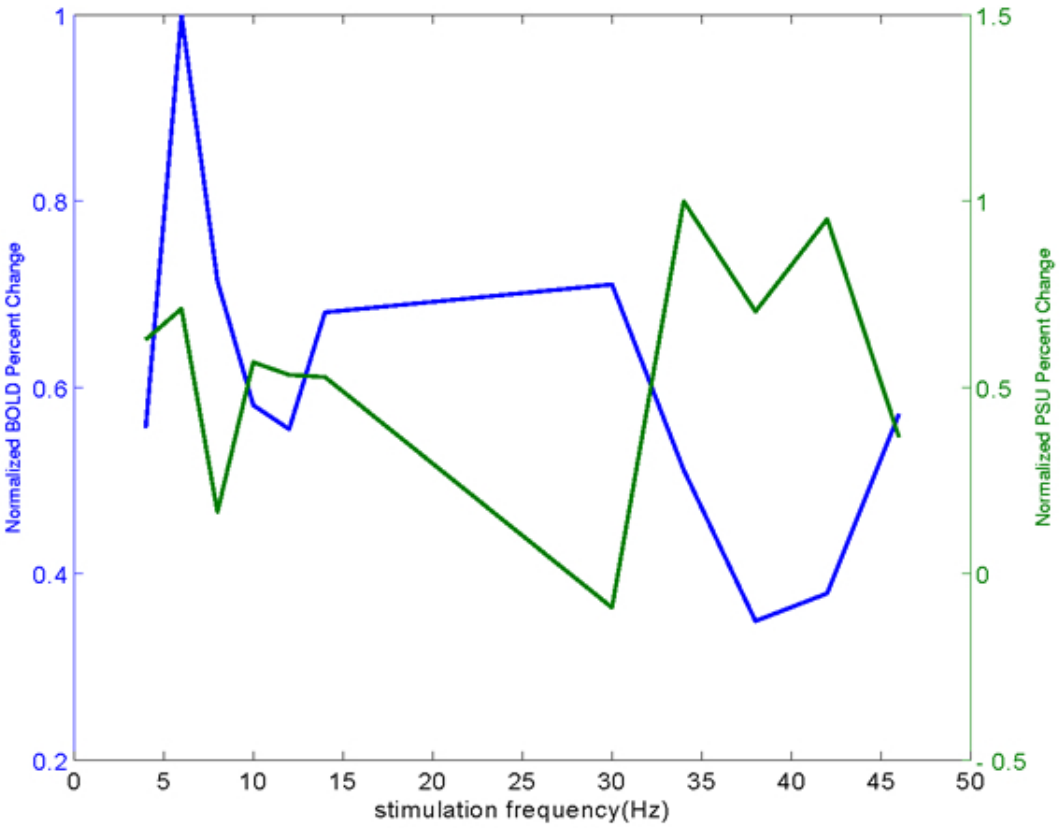

Figure 5.9 Normalized absolute PSU (Right y axis) and PBOLD (Left y axis) change across all frequencies. Maximum is set to 1.

6. DISCUSSION AND FUTURE WORK

The data shows that the post stimulus undershoot can have different magnitudes even when the positive BOLD response has relatively the same magnitude and time course. In this study static and flickering stimuli caused very similar overshoots at most of the frequencies, but only the flickering stimuli caused an undershoot. Also the flashing stimuli's post stimulus undershoot percentages vary with each frequency while the same positive BOLD time course, including the initial overshoot is visible for both the flashing and static stimuli.

Mandeville et al. have shown that a BOLD post stimulus undershoot is accompanied by a slow CBV recovery following stimulus termination [136]. Yacoub et al. demonstrated that the slow recovery of CBV was only present in gray matter but not in surface vessels, while BOLD undershoot could be found both in gray matter and surface vessels [138]. This indicates that the BOLD undershoot in surface layers reflects only the altered deoxyhemoglobin content of blood draining from the tissue where $CMRO_2$ and/or CBF effects must also contribute to the post stimulus time course of the HbR level. In this study, same voxels which were active in both the static and flickering stimuli were averaged. This ensured that the voxels had the same underlying vasculature. Therefore, as the positive responses are matched, the differences observed in the post stimulus undershoot responses can not be attributed solely to vascular composition or the CBV changes during stimulation. Taking this into consideration, it can be said that the CBF and/or the $CMRO_2$ must play a role in the observed undershoot, in addition to a passive biomechanical effect of blood vessel volume as proposed by the balloon model [98].

Also, very similar positive BOLD time courses for both the static and flashing stimuli can be seen in the resulting graphics. Thus one can assume this as the result of

very similar CBF, CBV and $CMRO_2$ magnitudes for both stimulus types for the period of stimulation. This is a reasonable assumption considering that the relationships between CBF-CBV and CBF-$CMRO_2$ have been shown to be constant during steady state [17]. Since the passive CBV component of the post stimulus undershoot in the veins is determined by the amplitude of the positive response and as the amplitude of the positive response was found to be nearly the same for both the flashing and static stimuli, either CBF or $CMRO_2$ effects can account for the following: a more pronounced CBF undershoot or a more elevated $CMRO_2$ level following the end of stimulus (Figure 6.1). Since both effects reflect neuronal activity [25, 26, 139, 140, 141, 142, 143, 144, 90, 91, 89, 145] , although the BOLD signal is an indirect reflection of neuronal activity it can be suggested that direct conclusions of the time course of neuronal activity may be possible following the post stimulus undershoot time course. So the PSU could also be caused in part by decreases in CBF triggered by the post stimulus decreases in neuronal activity [146].

As seen on Figure 5.9, there is no correlation between the positive BOLD and post stimulus undershoot responses changing with different stimulus frequencies. Also considering the suggestions on the paragraphs above, it can be proposed that the post stimulus undershoot of the BOLD signal has a frequency dependency independent of CBV changes. This suggests that the frequency dependency of PSU might be caused by neurally mediated metabolic activities such as $CMRO_2$ and CBF.

However this requires further investigation possibly with an addition of a method to account for the CBF measurements, such as the Arterial Spin Labeling (ASL) techniques. An addition of a PET protocol to the same procedure may also help in estimating the $CMRO_2$ in the subjects. Also tracking the subjects with an MR compatible EEG device could also help in pinpointing the results.

One problem I faced during experiments was caused by the lengthiness of the study. Each experiment for a frequency lasted for 7 and a half minutes. Multiplied

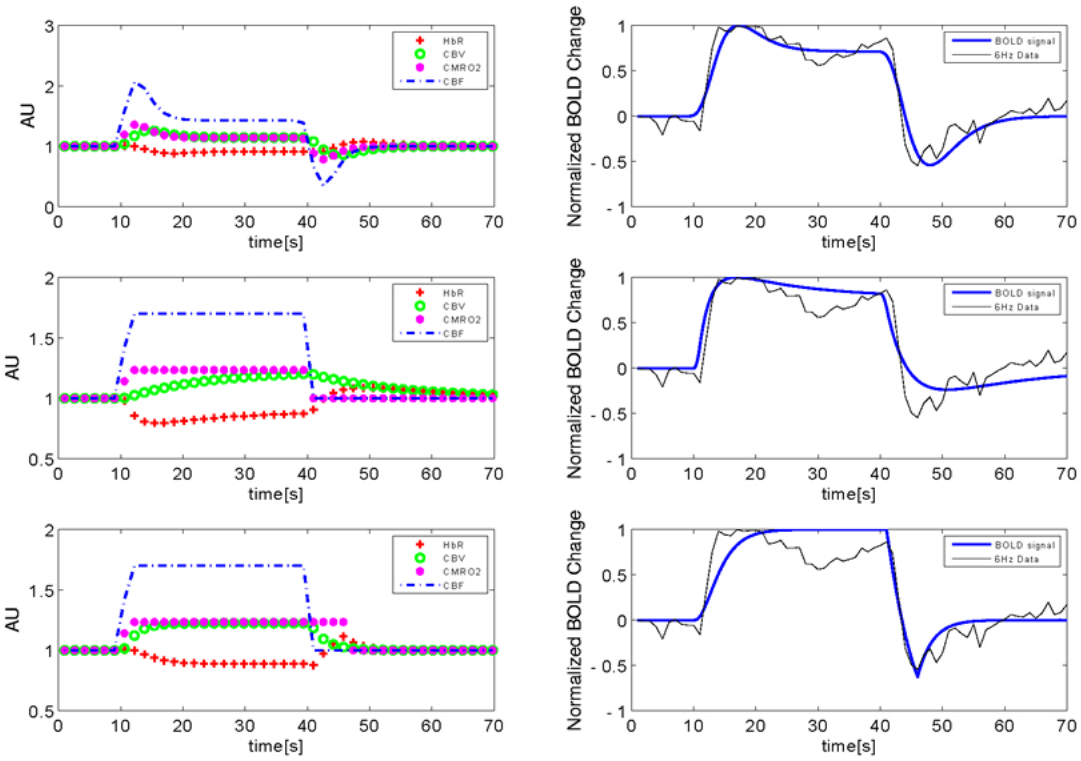

Figure 6.1 Application of the balloon model simulations on the 6Hz stimulus data with CBF, CBV and $CMRO_2$ effects on the post stimulus undershoot.

by 12 (for all of the flashing stimuli and one more for the static stimuli) totals to 90 minutes. Adding another 30 minutes accounting for the structural image acquisition as well as the small eye resting breaks requested by the subjects makes 120 minutes, whole 2 hours. So a stimulus length and type is required to get to the steady-state while not torturing subjects. The more time passes, the more the subjects get tired and uncomfortable which results in a reduced cooperation for the experiment as well as increased motion problems.

The availability of an MR machine is another problem. Although we have access to several hospitals' MR units -thanks to our instructors-, the time frames those MR machines available for non-patient studies are limited and sometimes interrupted by

unscheduled visits by patients. Conducting a study in which the full cooperation of the subject -at least keeping his/her eyes open- is necessary, does not go well with hours past midnight. Since it is not currently feasible to build a useful MR machine in our backyards, arrangement of subjects and precise dates beforehand for an experiment is necessary for future studies.

I had actually prepared another stimulus design -contrast enhanced flickering/static checkerboard- to be projected on a mirror via an LCD projector. In that study it would have been possible to track the CBF changes with the ASL Q2TIPS sequence as well as the BOLD signal changes. After 6 runs of the experiment with 6 different subjects, it was not possible to relate the resulting BOLD and CBF data due to a very bad SNR. Later we found out that the reason for that was faulty gradient coils of the machine which required fixing.

To sum up, a stimulus frequency dependency of the PSU is apparent which may reflect the differences in the hemodynamic coupling and/or in the neuronal activity based on the changing stimulus frequencies. The observed PSU amplitude changes can not solely be attributed to the changes in CBV, however a more thorough investigation which simultaneously measures the CBF can help to prove or disprove this observation. Also a multimodal investigation approach would help to account for the $CMRO_2$ and CBV changes at the same time.

REFERENCES

1. Dandy, W. E., "Roentgenography of the brain after the injection of air into the spinal canal.," *Ann Surg*, Vol. 70, pp. 397–403, 1919.

2. Maddison, I., *Radiology Database Website*, http://myweb.lsbu.ac.uk/dirt.

3. Malmivuo, J., and R. Plonsey, *Bioelectromagnetism: Principles and Applications of Bioelectric and Biomagnetic Fields*, Oxford: Oxford University Press, 1995.

4. LANL, *http://www.lanl.gov*, Los Alamos National Laboratory.

5. Dignazio, M., and A. Zamani, "Cerebral lymphoma," in *Online Teaching Cases*, http://brighamrad.harvard.edu/Cases/bwh/hcache/191/full.html: Department of Radiology, Brigham and Women's Hospital Harvard Medical School, Feb 1997.

6. Wikipedia, *http://en.wikipedia.org/wiki/Gamma_camera.*

7. BrainExplorer, *http://www.brainexplorer.org.*

8. McRobbie, D. W., E. A. Moore, M. J. Graves, and M. R. Prince, *MRI From Picture to Proton*, Cambridge UK: Cambridge University Press, 2nd ed., 2004.

9. Emir, U. E., *Multimodal Investigation of fMRI and fNIRS derived Breath Hold BOLD Signals with an Expanded Balloon Model.* PhD thesis, Bogazici University, Istanbul, Turkey, 2008.

10. Tarnanen, I., "Electroencephalography in a 3-t magnetic resonance imaging scanner.," Master's thesis, Helsinki University of Technology, Helsinki, 2005.

11. FreeThoughtForum, *http://www.freethought-forum.com/.*

12. Pellerin, L., and P. J. Magistretti, "Food for thought: challenging the dogmas.," *J Cereb Blood Flow Metab*, Vol. 23, pp. 1282–1286, Nov 2003.

13. Sidaraos, K., *Slice profile effects in MR perfusion imaging using pulsed Arterial Spin Labeling.* PhD thesis, Technical University of Denmark, Denmark, 2002.

14. Amano, T., "A brief review of dr f gotoh's contribution to neuroscience: research in the field of cerebral blood flow and stroke.," *Keio J Med*, Vol. 50, pp. 72–80, 2001.

15. Buxton, R. B., *Introduction to Functional Magnetic Resonance Imaging Principles & Techniques*, Cambridge UK: Cambridge University Press, 2002.

16. Ogawa, S., T. M. Lee, A. R. Kay, and D. W. Tank, "Brain magnetic resonance imaging with contrast dependent on blood oxygenation.," *Proc Natl Acad Sci USA*, Vol. 87, pp. 9868–9872, 1990.

17. Buxton, R. B., K. Uludag, D. J. Dubowitz, and T. T. Liu, "Modeling the hemodynamic response to brain activation.," *Neuroimage*, Vol. 23, pp. 220–233, 2004.

18. Obata, T., T. T. Liu, K. L. Miller, W. M. Luh, E. C. Wong, L. R. Frank, and R. B. Buxton, "Discrepancies between bold and flow dynamics in primary and supplementary motor areas: application of the balloon model to the interpretation of bold transients.," *Neuroimage*, Vol. 21, pp. 144–153, Jan 2004.

19. Mandeville, J. B., J. J. A. Marota, B. E. Kosofsky, J. R. Keltner, R. Weissleder, B. R. Rosen, and R. M. Weisskoff, "Dynamic functional imaging of relative cerebral blood volume during rat forepaw stimulation.," *Magn Reson Med*, Vol. 39, pp. 615–624, 1998.

20. Kwong, K. K., J. W. Belliveau, D. A. Chesler, I. E. Goldberg, R. M. Weisskoff, B. P. Poncelet, D. N. Kennedy, B. E. Hoppel, M. S. Cohen, and R. T. R, "Dynamic magnetic resonance imaging of human brain activity during primary sensory stimulation.," *Proc Natl Acad Sci USA*, Vol. 89, pp. 5675–5679, Jun 1992.

21. Ozus, B., H. L. Liu, L. Chen, M. B. Iyer, P. T. Fox, and J. H. Gao, "Rate dependence of human visual cortical response due to brief stimulation: an event-related fmri study.," *Magn Reson Imaging*, Vol. 19, pp. 21–25, Jan 2001.

22. Singh, M., S. Kim, and T. Kim, "Correlation between bold-fmri and eeg signal changes in response to visual stimulus frequency in humans.," *Magn Reson Med*, Vol. 49, pp. 108–114, Jan 2003.

23. Thomas, C. G., and R. S. Menon, "Amplitude response and stimulus presentation frequency response of human primary visual cortex using bold epi at 4 t.," *Magn Reson Med*, Vol. 40, pp. 203–209, Aug 1998.

24. Zhu, X. H., S. G. Kim, P. Andersen, S. Ogawa, K. Ugurbil, and W. Chen, "Simultaneous oxygenation and perfusion imaging study of functional activity in primary visual cortex at different visual stimulation frequency: quantitative correlation between bold and cbf changes.," *Magn Reson Med*, Vol. 40, pp. 703–711, 1998.

25. Fox, P. T., and M. E. Raichle, "Stimulus rate dependence of regional cerebral blood flow in human striate cortex, demonstrated by positron emission tomography.," *J Neurophysiol*, Vol. 51, pp. 1109–1120, 1984.

26. Fox, P. T., and M. E. Raichle, "Stimulus rate determines regional brain blood flow in striate cortex.," *Ann Neurol*, Vol. 17, pp. 303–305, 1985.

27. Fulton, J. F., "Observations upon the vascularity of the human occipital lobe during visual activity.," *Brain*, Vol. 51, pp. 310–320, 1928.

28. Kety, S. S., and C. F. Schmidt, "Nitrous oxide method for quantitative determination of cerebral blood flow in man: Theory, procedure and normal values.," *J Clin Invest*, Vol. 27, pp. 475–483, 1948.

29. Kety, S. S., "The theory and applications of the exchange of inert gas at the lungs and tissues.," *Pharmacol Rev*, Vol. 3, pp. 1–14, 1951.

30. Landau, W. M., W. H. Freygang, L. P. Roland, L. Sokoioff, and S. S. Kety, "The local circulation of the living brain: values in the unanesthetized and anesthetized cat.," *Trans Am Neuro Assoc*, Vol. 80, pp. 125–129, 1955.

31. Caton, R., "The electric currents of the brain.," *British Med J*, Vol. 2, p. 278, 1875.

32. Berger, H., "Über das elektroenkephalogramm des menschen.," *Archiv Psychatrie Nervenkr*, Vol. 87, pp. 527–550, 1929.

33. Finger, S., *Origins of Neuroscience*, New York: Oxford University Press, 1994.

34. Okada, Y., *Biomagnetism: an Interdisciplinary Approach. ch: Neurogenesis of evoked magnetic fields.*, Plenum Press, 1983.

35. Maxwell, J. C., "On physical lines of force.," *The London, Edinburgh and Dublin Philosophical Magazine and Journal of Science*, Vol. 4, 1861.

36. Cohen, D., "Magnetoencephalography: evidence of magnetic fields produced by alpha rhythm currents.," *Science*, Vol. 161, pp. 784–786, 1968.

37. Cohen, D., "Magnetoencephalography: Detection of the brain's electrical activity with a superconducting magnetometer.," *Science*, Vol. 175, pp. 664–666.

38. Sutherling, W. W., P. H. Crandall, T. M. Darcey, D. P. Becker, M. F. Levesque, and D. S. Barth, "The magnetic and electric fields agree with intracranial localizations of somatosensory cortex.," *Neurology*, Vol. 38, pp. 1705–1714, 1988.

39. Rowley, H. A., and T. P. Roberts, "Functional localization by magnetoencephalography.," *Neuroimaging Clin North Am*, Vol. 5, pp. 695–710, 1995.

40. Gallen, C. C., E. C. Hirschkoff, and D. S. Buchanan, "Magnetoencephalography and magnetic source imaging: Capabilities and limitations.," *Neuroimaging Clin North Am*, Vol. 5, pp. 227–249, 1995.

41. Hounsfield, G. N., "Computed transverse axial scanning (tomography). part 1: Description of system.," *Br J Radiol*, 1973.

42. Kak, A. C., and M. Slaney, *Principles of Computerized Tomographic Imaging.*, New York: IEEE Press, 1998.

43. Dougnal, N. J., S. Bruggink, and K. P. Ebmeier, "Systematic review of the diagnostic accuracy of 99mtc-hmpao-spect in dementia.," *Am J Geriatr Psychiatry*, Vol. 12, pp. 554–70, Nov-Dec 2004.

44. Bonte, F. J., T. S. Harris, L. S. Hynan, E. H. Bigio, and C. L. W. 3rd, "Tc-99m hmpao spect in the differential diagnosis of the dementias with histopathologic confirmation.," *Clin Nucl Med*, Vol. 31, pp. 376–8, Jul 2006.

45. Ter-Pogossian, M. M., M. E. Phelps, E. J. Hoffman, and N. A. Mullani, "Positron-emission transaxial tomograph for nuclear imaging (pett).," *Radiology*, Vol. 114, no. 1, pp. 89–98, 1975.

46. Fox, P. T., M. A. Mintun, M. E. Raichle, and P. Herscovitch, "A noninvasive approach to quantitative functional brain mapping with h215o and positron emission tomography.," *J. Cereb. Blood Flow Metab.*, Vol. 4, pp. 329–333, 1984.

47. Magistretti, P. J., and L. Pellerin, "Cellular basis of brain energy metabolism and their relevance to functional brain imaging: evidence for a primary role of astrocytes.," *Cerebral Cortex*, Vol. 6, pp. 50–61, 1996.

48. Toyama, H., M. Ichise, J. S. Liow, K. J. Modell, D. C. Vines, T. Esaki, M. Cook, J. Seidel, L. Sokolo, M. V. Green, and R. B. Innis, "Absolute quantification of regional cerebral glucose utilization in mice by 18f-fdg small animal pet scanning and 2-14c-dg autoradiography.," *J Nucl Med*, Vol. 45, pp. 1398–1405, Aug 2004.

49. Purcell, E. M., H. C. Torrey, and R. V. Pound, "Resonance absorption by nuclear magnetic moments in a solid.," *Phys. Rev.*, Vol. 69, no. 37–38, 1946.

50. Bloch, F., W. W. Hansen, and M. Packard, "Nuclear induction.," *Phys. Rev.*, Vol. 69, p. 127, 1946.

51. Hahn, E. L., "Spin echoes.," *Phys. Rev.*, Vol. 80, pp. 580–594, Nov 1950.

52. Damadian, R., "Tumor detection by nuclear magnetic resonance.," *Science*, Vol. 171, pp. 1151–1153, Mar 1971.

53. Lauterbur, P. C., "Image formation by induced local interactions: Examples employing nuclear magnetic resonance.," *Nature*, Vol. 242, pp. 190–191, 1973.

54. Damadian, R., L. Minkoff, M. Goldsmith, M. Stanford, and J. Koutcher, "Field focusing nuclear magnetic resonance (fonar): visualization of a tumor in a live animal.," *Science*, Vol. 194, no. 4272, pp. 1430–1432, 1976.

55. Damadian, R., M. Goldsmith, and L. Minkoff, "Fonar image of the live human body.," *Physiol Chem & Phys*, Vol. 9, pp. 97–100, 1977.

56. Ritter, P., and A. Villringer, "Simultaneous eeg-fmri.," *Neurosci Biobehav Rev*, Vol. 30, no. 6, pp. 823–838, 2006.

57. Emir, U. E., C. Ozturk, and A. Akin, "Multimodal investigation of fmri and fnirs derived breath hold bold signals with an expanded balloon model.," *Physiol Meas*, Vol. 29, pp. 49–63, 2008.

58. Siesjo, B. K., *Brain Energy Metabolism*, New York: Wiley, 1978.

59. Blaustein, M. P., "Calcium transport and buffering in neurons.," *Trends Neurosci.*, Vol. 11, pp. 438–443.

60. Magistretti, P. J., L. Pellerin, D. L. Rothman, and R. G. Shulman, "Energy on demand.," *Science*, Vol. 283, pp. 496–497, Jan 1999.

61. Oldendorf, W. H., "Brain uptake of radiolabeled amino acids, amines, and hexoses after arterial injection.," *Am J Physiol*, Vol. 22, pp. 1629–1639, 1971.

62. Gjedde, A., "Does deoxyglucose uptake in the brain reflect energy metabolism?," *Biochem Pharmacol*, Vol. 36, pp. 1853–61, 1987.

63. Sokoloff, L., "Relation between physiological function and energy metabolism in the central nervous system.," *J Neurochem*, Vol. 29, pp. 13–26, 1977.

64. Sokoloff, L., M. Reivich, C. Kennedy, M. H. D. Rosiers, C. S. Patlak, K. D. Pettigrew, O. Sakurada, and M. Shinohara, "The [14-c]deoxyglucose method for the measurement of local cerebral glucose utilization: Theory procedure and normal values in the conscious and anesthetized albino rat.," *J Neurochem*, Vol. 28, pp. 897–916, 1977.

65. Kennedy, C., M. H. D. Rosiers, O. Sakurada, M. Shinohara, M. Reivich, J. W. Jehle, and L. Sokoloff, "Metabolic mapping of the primary visual system of the monkey by means of the autoradiographic [14c]deoxyglucose technique.," *Proc Natl Acad Sci USA*, Vol. 73, pp. 4230–4234, 1976.

66. Schwartz, W. J., C. B. Smith, L. Davidsen, H. Savaki, L. Sokoloff, M. Mata, D. J. Fink, and H. Gainer, "Metabolic mapping of functional activity in the hypothalamo-neurohyhophysial system of the rat.," *Science*, Vol. 205, pp. 723–725, 1979.

67. Sokoloff, L., "The relation between function and energy metabolism: its use in the localization of functional activity in the nervous system.," *Neurosci Res Prog Bull*, Vol. 19, pp. 159–210, 1981.

68. Phelps, M. E., and J. C. Mazziotta, "Postiron emission tomography: human brain function and biochemistry.," *Science*, Vol. 228, pp. 799–809, 1985.

69. Tsacopoulos, M., and P. J. Magistretti, "Metabolic coupling between glia and neurons.," *J Neurosci*, Vol. 16, pp. 877–885, 1996.

70. Pawlik, G., A. Rackl, and R. J. Bing, "Quantitative capillary topography and blood flow in the cerebral cortex of cats: An in vivo microscopic study.," *Brain Res*, Vol. 208, pp. 35–58, 1981.

71. Villringer, A., A. Them, U. Lindauer, K. Einhaupl, and U. Dirnagl, "Capillary perfusion of the rat brain cortex: An in vivo confocal microscopy study.," *Circ Res*, Vol. 75, pp. 55–62, 1994.

72. Yang, S. P., and J. A. Krasny, "Cerebral blood flow and metabolic responses to sustained hypercapnia in awake sheep.," *J Cereb Blood Flow Metabol*, Vol. 15, pp. 115–23, 1995.

73. Ingvar, D. H., and N. H. Lassen, "Regional blood flow of the cerebral cortex determined by 85-krypton.," *Acta Physiol Scand*, Vol. 54, pp. 325–338, 1963.

74. Obrist, W. D., H. K. Thompson, C. H. King, and H. S. Wang, "Determination of regional cerebral blood flow by inhalation of 133-xenon.," *Circulation Res*, Vol. 20, pp. 124–135, 1967.

75. Frackowiak, R. S. J., G. L. Lenzi, T. Jones, and J. D. Heather, "Quantitative measurement of cerebral blood flow and oxygen metabolism in man using 15o and pet: Theory, procedure and normal values," *J Comput Assist Tomogr*, Vol. 4, pp. 727–736, 1980.

76. Raichle, M. E., "Brain blood flow measured with intravenous h2150: Implementation and validation.," *J Nucl Med*, Vol. 24, pp. 790–798, 1983.

77. Bernstein, M. A., K. F. King, and X. J. Zhou, *Handbook of MRI Pulse Sequences*, Elsevier, 2004.

78. Grubb, R. L., M. E. Raichle, J. O. Eichling, and M. M. Ter-Pogossian, "The effects of changes in pco2 on cerebral blood volume, blood flow, and vascular mean transit time.," *Stroke*, Vol. 5, pp. 630–639, 1974.

79. Lassen, N. A., *Cations as mediators of functional hyperemia in the brain. In: Brain work and mental activity.*, 1991.

80. Dirnagl, U., K. Niwa, U. Lindauer, and A. Villringer, "Coupling of cerebral blood flow to neuronal activation: Role of adenosine and nitric oxide.," *Am J Physiol*, Vol. 267, pp. 296–301, 1994.

81. Winn, H. R., A. C. Ngai, and K. R. Ko, *Role of adenosine in regulating microvascular CBF in activated sensory cortex. In: Brain work and mental activity: Quantitative studies with radioactive tracers.*, 1991.

82. Iadecola, J., "Regulation of cerebral microcirculation during neural activity: Is nitric oxide the missing link?," *TINS*, Vol. 16, pp. 206–214, 1993.

83. Watkins, L. D., "Nitric oxide and cerebral blood flow: An update.," *Cerebrovascular and Brain Metabolism Reviews*, Vol. 7, pp. 324–337, 1995.

84. Villringer, A., and U. Dirnagle, "Coupling brain activity and cerebral blood flow: Basis of functional neuroimaging.," *Cerebrovascular and Brain Metabolism Reviews*, Vol. 7, pp. 240–276, 1995.

85. Fox, P. T., and M. E. Raichle, "Focal physiological uncoupling of cerebral blood flow and oxidative metabolism during somatosensory stimulation in human subjects.," *Proc Natl Acad Sci USA*, Vol. 83, pp. 1140–1144, 1986.

86. Marchall, G., P. Rioux, M. C. Petit-Taboue, G. Sette, J. M. Travere, C. LePoec, P. Courtheoux, J. M. Derlon, and J. C. Baron, "Regional cerebral oxygen consumption, blood flow, and blood volume in healthy human aging.," *Arch Neurol*, Vol. 49, pp. 1013–1020, 1992.

87. Prichard, J., D. Rothman, E. Novotny, O. Petroff, T. Kuwabara, M. Avison, A. Howseman, C. Hanstock, and R. Shulman, "Lactate rise detected by 1h nmr in human visual cortex during physiologic stimulation.," *Proc Natl Acad Sci USA*, Vol. 88, pp. 5829–5831, 1991.

88. Sappey-Marinier, D., G. Calabrese, G. Fein, J. W. Hugg, C. Biggins, and M. W. Weiner, "Effect of photic stimulation on human visual cortex lactate and phosphates using 1h and

31p magnetic resonance spectroscopy.," *J Cereb Blood Flow Metabol*, Vol. 12, pp. 584–592, 1992.

89. Davis, T. L., K. K. Kwong, R. M. Weisskoff, and B. R. Rosen, "Calibrated functional mri: Mapping the dynamics of oxidative metabolism.," *Proc Natl Acad Sci USA*, Vol. 95, pp. 1834–1839, 1998.

90. Hoge, R. D., J. Atkinson, B. Gill, G. R. Crelier, S. Marrett, and G. B. Pike, "Investigation of bold signal dependence on cerebral blood flow and oxygen consumption: The deoxyhemoglobin dilution model.," *Magn Reson Med*, Vol. 42, pp. 849–863, 1999.

91. Hoge, R. D., J. Atkinson, B. Gill, G. R. Crelier, S. Marrett, and G. B. Pike, "Linear coupling between cerebral blood flow and oxygen consumption in activated human cortex.," *Proc Natl Acad Sci USA*, Vol. 96, pp. 9403–9408, 1999.

92. Buxton, R. B., and L. R. Frank, "A modal for the coupling between cerebral blood flow and oxygen metabolism during neural stimulation.," *J Cereb Blood Flow Metabol*, Vol. 17, pp. 64–72, 1997.

93. Gjedde, A., S. Ohta, H. Kuwabara, and E. Meyer, *Is oxygen diffusion limiting for blood-brain transfer of oxygen? In: Brain work and mental activity.*, 1991.

94. Kassissia, I. G., C. A. Goresky, C. P. Rose, A. J. Schwab, A. Simard, P.-M. Huet, and G. G. Bach, "Tracer oxygen distribution is barrier-limited in the cerebral microcirculation," *Circulation Res*, Vol. 77, pp. 1201–1211, 1995.

95. Bereczki, D., L. Wei, T. Otsuka, V. Acuff, K. Pettigrew, C. Patlak, and J. Fenstermacher, "Hypoxia increased velocity of blood flow through paranchymal microvascular systems in rat brain.," *J Cereb Blood Flow Metabol*, Vol. 13, no. 3, pp. 475–486, 1993.

96. Gobel, U., H. Theilen, and W. Kuschinsky, "Congruence of total and perfused capillary network in rat brains.," *Circulation Res*, Vol. 66, pp. 271–281, 1990.

97. Frahm, J., G. Krueger, K. D. Merboldt, and A. Kleinschmidt, "Dynamic uncoupling and recoupling of perfusion and oxidative metabolism during focal activation in man.," *Magn Reson Med*, Vol. 35, pp. 143–148, 1996.

98. Buxton, R. B., E. C. Wong, and L. R. Frank, "Dynamics of blood flow and oxygenation changes during brain activation: The balloon model.," *Magn Reson Med*, Vol. 39, pp. 855–864, 1998.

99. Belliveau, J. W., D. N. K. Jr, R. C. McKinstry, B. R. Buchbinder, R. M. Weisskoff, M. S. Cohen, J. M. Vevea, T. J. Brady, and B. R. Rosen, "Functional mapping of the human visual cortex by magnetic resonance imaging.," *Science*, Vol. 254, no. 5032, pp. 716–719, 1991.

100. Thulborn, K. R., J. C. Waterton, P. M. Matthews, and G. K. Radda, "Oxygenation dependence of the transverse relaxation time of water protons in whole blood at high field.," *Biochem Biophy Acta*, Vol. 714, pp. 265–270, 1982.

101. Ogawa, S., T. M. Lee, A. S. Nayak, and P. Glynn, "Oxygenation - sensitive contrast in magnetic resonance image of rodent brain at high magnetic fields.," *Magn Reson Med*, Vol. 14, pp. 68–78, 1990.

102. Turner, R., D. LeBihan, C. T. W. Moonen, D. Despres, and J. Frank, "Echo-planar time course mri of cat brain oxygenation changes.," *Magn Reson Med*, Vol. 27, pp. 159–166, 1991.

103. Bandettini, P. A., E. C. Wong, R. S. Hinks, R. S. Tikofsky, and J. S. Hyde, "Time course epi of human brain function during task activation.," *Magn Reson Med*, Vol. 25, pp. 390–397, 1992.

104. Frahm, J., H. Bruhn, K. D. Merboldt, W. Hanicke, and D. Math, "Dynamic mr imaging of human brain oxgenation during rest and photic stimulation.," *J Magn Reson Imag*, Vol. 2, pp. 501–505, 1992.

105. Ogawa, S., D. W. Tank, R. Menon, J. M. Ellermann, S. G. Kim, H. Merkle, and K. Ugurbil, "Intrinsic signal changes accompanying sensory stimulation: Functional brain mapping with magnetic resonance imaging.," *Proc Natl Acad Sci USA*, Vol. 89, pp. 5951–5955, Jul 1992.

106. Boxerman, J. L., P. A. Bandettini, K. K. Kwong, J. R. Baker, T. L. Davis, B. R. Rosen, and R. M. Weissko, "The intravascular contribution to fmri signal change: Monte carlo

modeling and diffusion-weighted studies in vivo," *Magn Reson Med*, Vol. 34, pp. 4–10, Jul 1995.

107. Song, A. W., E. C. Wong, S. G. Tan, and J. S. Hyde, "Diffusion weighted fmri at 1.5t.," *Magn Reson Med*, Vol. 35, pp. 155–158, Feb 1996.

108. Buxton, R. B., W. M. Luh, E. C. Wong, L. R. Frank, and P. A. Bandettini, "Diffusion-weighted attenuates the bold peak signal change but not the post-stimulus undershoot.," in *ISMRM*, p. 7, 1998.

109. Song, A. W., H. Fichtenholtz, and M. Woldor, "Bold signal compartmentalization based on the apparent diffusion coefficient.," *Magn Reson Imaging*, Vol. 20, pp. 521–525, Sep 2002.

110. Menon, R. S., "Postacquisition suppression of large-vessel bold signals in high-resolution fmri.," *Magn Reson Med*, Vol. 47, pp. 1–9, Jan 2002.

111. Edelman, R. R., B. Siewert, D. G. Darby, V. Thangaraj, A. C. Nobre, M. M. Mesulam, and S. Warach, "Qualitative mapping of cerebral blood flow and functional localization with echo-planar mr imaging and signal targeting with alternating radio frequency.," *Radiology*, Vol. 192, pp. 513–520, Aug 1994.

112. Edelman, R. R., and Q. Chen, "Epistar mri: multislice mapping of cerebral blood flow.," *Magn Reson Med*, Vol. 40, pp. 800–805, Dec 1998.

113. Luh, W. M., E. C. Wong, P. A. Bandettini, and J. S. Hyde, "Quipss ii with thin-slice ti1 periodic saturation: a method for improving accuracy of quantitative perfusion imaging using pulsed arterial spin labeling.," *Magn Reson Med*, Vol. 41, pp. 1246–1254, Jun 1999.

114. Wong, E. C., W. M. Luh, and T. T. Liu, "Turbo asl: arterial spin labeling with higher snr and temporal resolution.," *Magn Reson Med*, Vol. 44, pp. 511–515, Oct 2000.

115. Tuunanen, P. I., and R. A. Kauppinen, "Effects of oxygen saturation on bold and arterial spin labeling perfusion fmri signals studied in a motor activation task.," *Neuroimage*, Vol. 20, pp. 102–109, 2006.

116. Logothetis, N. K., J. pauls, M. Augath, T. Trinath, and A. Oeltermann, "Neurophysiological investigation of the basis of the fmri signal.," *Nature*, Vol. 412, pp. 150–157, Jul 2001.

117. Malonek, D., and A. Grinvald, "Interactions between electrical activity and cortical microcirculation revealed by imaging spectroscopy: implications for functional brain mapping.," *Science*, Vol. 272, pp. 551–554, Apr 1996.

118. Fransson, P., G. Krueger, K. D. Melboldt, and J. Frahm, "Temporal characteristics of oxgenation-sensitive mri responses to visual activation in humans.," *Magn Reson Med*, Vol. 39, pp. 912–919, 1998.

119. Yacoub, E., and X. Hu, "Detection of the early negative response in fmri at 1.5t.," *magn Reson Med*, Vol. 41, pp. 1088–1092, 1999.

120. Hathout, G. M., B. Varjavand, and R. K. Gopi, "The early response in fmri: a modeling approach.," *Magn Reson Med*, Vol. 41, pp. 550–554, Mar 1999.

121. Kohl, M., U. Lindauer, G. Royl, M. Kuhl, L. Gold, A. Villringer, and U. Dirnagl, "Physical model for the spectroscopic analysis of cortical intrinsic optical signals.," *Phys Med Biol*, Vol. 45, pp. 3749–3764, 2000.

122. Mildner, T., D. G. Norris, C. Schwarzbauer, and C. J. Wiggins, "A qualitative test of the balloon model for bold-based mr signal changes at 3t.," *Magn Reson Med*, Vol. 46, pp. 891–899, Nov 2001.

123. Moonen, C. T. W., and P. A. Bandettini, *Functional MRI*, Springer, 2000.

124. Krueger, G., A. Kleinschmidt, and J. Frahm, "Dynamic mri sensitized to cerebral blood oxygenation and flow during sustained activation of human visual cortex.," *Magn Reson Med*, Vol. 35, pp. 797–800, 1996.

125. Schroeter, M. L., T. Kupka, T. Mildner, K. Uludag, and D. Y. von Cramon, "Investigating the post-stimulus undershoot of the bold signal. a simultaneous fmri and fnirs study.," *Neuroimage*, Vol. 30, pp. 349–358, Apr 2006.

126. Buxton, R. B., K. Miller, L. R. Frank, and E. C. Wong, "Bold signal dynamics: The balloon model with viscoelastic effects.," in *ISMRM*, p. 1401, 1998.

127. Hoge, R. D., J. Atkinson, B. Gill, G. R. Crelier, S. Marrett, and G. B. Pike, "Stimulus dependent bold and perfusion dynamics in human v1.," *Neuroimage*, Vol. 9, pp. 573–585, Jun 1999.

128. Uludag, K., D. J. Dubowitz, E. J. Yoder, K. Restom, T. T. Liu, and R. B. Buxton, "Coupling of cerebral blood flow and oxygen consumption during physiological activation and deactivation measured with fmri.," *Neuroimage*, Vol. 23, pp. 148–155, Sep 2004.

129. Liu, T. T., Y. Behzadi, K. Restom, K. Uludag, K. Lu, G. T. Buracas, D. J. Dubowitz, and R. B. Buxton, "Caffeine alters the temporal dynamics of the visual bold response.," *Neuroimage*, Vol. 23, pp. 1402–1413, Dec 2004.

130. Davis, T. L., R. M. Weisskoff, K. K. Kwong, R. Savoy, and B. R. Rosen, "Susceptibility contrast undershoot is not matched by inflow contrast undershoot.," in *SMR*, p. 435, 1994.

131. Buxton, R. B., K. Miller, E. C. Wong, and L. R. Frank, "Application of the balloon model to the bold response to stimuli of different duration.," in *ISMRM*, p. 1735, 1999.

132. Krueger, G., A. Kleinschmidt, and J. Frahm, "Stimulus dependence of oxygenationsensitive mri responses to sustained visual activation.," *NMR Biomed*, Vol. 11, pp. 75–79, Apr 1998.

133. Krueger, G., P. Fransson, K. D. Merboldt, and J. Frahm, "Does stimulus quality affect the physiologic mri responses to brief visual activation?," *Neuroreport*, Vol. 10, pp. 1277–1281, Apr 1999.

134. Lu, H., X. Golay, J. J. Pekar, and P. C. M. van Zijl, "Sustained poststimulus elevation in cerebral oxygen utilization after vascular recovery.," *Cereb Blood Flow Metab*, Vol. 24, pp. 764–770, Jul 2004.

135. Mandeville, J. B., J. J. A. Marota, C. Ayata, M. A. Moskowitz, R. M. Weisskoff, and B. R. Rosen, "Mri measurement of the temporal evolution of relative cmro2 during rat forepaw stimulation.," *Magn Reson Med*, Vol. 42, pp. 944–951, 1999.

136. Mandeville, J. B., J. J. A. Marota, C. Ayata, G. Zaharchuk, M. A. Moskowitz, B. R. Rosen, and R. M. Weisskoff, "Evidence of a cerebrovascular postarteriole windkessel with delayed compliance," *J Cereb Blood Flow Metabol*, Vol. 19, pp. 679–689, 1999.

137. Cox, R. W., "Afni: Software for analysis and visualization of functional magnetic resonance neuroimages.," *Comput Biomed Res*, Vol. 29, pp. 162–173, Jun 1996.

138. Yacoub, E., K. Ugurbil, and N. Harel, "The spatial dependence of the poststimulus undershoot as revealed by high-resolution bold- and cbv-weighted fmri.," *J Cereb Blood Flow Metabol*, Vol. 26, pp. 634–644, 2006.

139. Blinkenberg, M., C. Bonde, S. Holm, C. Svarer, J. Andersen, O. B. Paulson, and I. Law, "Rate dependence of regional cerebral activation during performance of a repetitive motor task: A pet study.," *J Cereb Blood Flow Metabol*, Vol. 16, pp. 794–803, 1996.

140. Price, C., R. Wise, S. Ramsay, K. Friston, D. Howard, K. patterson, and R. Frackowiak, "Regional response differences within the human auditory cortex when listening to words.," *Neurosci Lett*, Vol. 146, pp. 179–182, 1992.

141. Marrett, S., and A. Gjedde, "Changes of blood flow and oxygen consumption in visual cortex of living humans.," *Adv Exp Med Biol*, Vol. 413, pp. 205–208, 1997.

142. Seitz, R. J., and P. E. Roland, "Vibratory stimulation increases and decreases the regional cerebral blood flow and oxidative metabolism: A positron emission tomography (pet) study.," *Acta Neurol Scand*, Vol. 86, pp. 60–67, 1992.

143. Vafaee, M., S. Marrett, E. Meyer, A. C. Evans, and A. Gjedde, "Increased oxygen consumption in human visual cortex: response to visual stimulation.," *Acta Neurol Scand*, Vol. 98, pp. 85–89, 1998.

144. Vafaee, M., E. Meyer, S. Marrett, T. Paus, A. C. Evans, and A. Gjedde, "Frequency-dependent changes in cerebral metabolic rate of oxygen during activation of human visual cortex.," *J Cereb Blood Flow Metabol*, Vol. 19, pp. 272–277, 1999.

145. Kim, S. G., E. Rostrup, H. B. W. Larsson, S. Ogawa, and O. B. Paulson, "Determination of relative cmro2 from cbf and bold changes: Significant increase of oxygen consumption rate during visual stimulation.," *Magn Reson Med*, Vol. 41, pp. 1152–1161, 1999.

146. Shmuel, A., M. Augath, A. Oeltermann, and N. K. Logothetis, "Negative functional mri response correlates with decreases in neuronal activity in monkey visual area v1.," *Nature*, Vol. 9, pp. 569–577, Apr 2006.